# Materials, physics and systems for multicaloric cooling

*Huilong Hou*[1,2,6]✉, *Suxin Qian*[3,6] *and Ichiro Takeuchi*[4,5]✉

Abstract | Calls to minimize greenhouse gas emissions and demands for higher energy efficiency continue to drive research into alternative cooling and refrigeration technologies. The caloric effect is the reversible change in temperature and entropic states of a solid material subjected to one or more fields and can be exploited to achieve cooling. The field of caloric cooling has undergone a series of transformations over the past 50 years, bolstered by the advent of new materials and devices, and these developments have contributed to the emergence of multicalorics in the past decade. Multicaloric materials display one or more types of ferroic order that can give rise to multiple field-induced phase transitions that can enhance various aspects of caloric effects. These materials could open up new avenues for extracting heat and spearhead hitherto unknown technological applications. In this Review, we survey the emerging field of multicaloric cooling and explore state-of-the-art caloric materials and systems (devices) that are responsive to multiple fields. We present our vision of the future applications of multicaloric and caloric cooling and examine key factors that govern the overall system efficiency of the cooling devices.

[1]*Institute of Solid Mechanics, School of Aeronautic Science and Engineering, Beihang University, Beijing, People's Republic of China.*

[2]*Beihang Hangzhou Innovation Institute (Yuhang District), Hangzhou, People's Republic of China.*

[3]*Department of Refrigeration and Cryogenic Engineering, Xi'an Jiaotong University, Xi'an, People's Republic of China.*

[4]*Department of Materials Science and Engineering, University of Maryland, College Park, MD, USA.*

[5]*Maryland Quantum Materials Center, Department of Physics, University of Maryland, College Park, MD, USA.*

[6]*These authors contributed equally: Huilong Hou, Suxin Qian.*

✉*e-mail: huilong_hou@buaa.edu.cn; takeuchi@umd.edu*

https://doi.org/10.1038/s41578-022-00428-x

The cooling technologies ubiquitous in modern society account for a considerable fraction of worldwide energy consumption and greenhouse gas emissions. Space cooling and refrigeration based on vapour compression consume ~20% of all electricity generated[1], and some commonly used refrigerants have a global warming potential a thousandfold greater than that of $CO_2$. The two-centuries-old vapour-compression technology is highly optimized and efficient, but calls to minimize greenhouse gas emissions and demands for even higher energy efficiency are driving research into alternative cooling and refrigeration technologies.

Leading alternative cooling technologies include those based on caloric materials, which are solid materials that undergo reversible phase transitions and exhibit field-induced temperature changes. Caloric materials that are responsive to magnetic, electric or stress fields are termed magnetocaloric, electrocaloric or mechanocaloric, respectively[2–8]. Cooling technologies based on caloric materials derive heat-pumping capabilities from the manipulation of internal order parameters. Caloric materials exhibit high energy-conversion efficiencies and do not emit greenhouse gases. Over the past 10 years, there has been a steady increase in the variety of caloric materials and prototype devices[9–16].

A particularly exciting new direction is multicaloric materials[2,3,17–19], which exhibit ferroic order(s) near a first-order transition in response to more than one external field. Such caloric materials can possess coexisting and/or coupled ferroic order parameters, and an emerging trend is multicaloric cooling, whereby multiple fields (magnetic, electric or stress) are applied to a multicaloric material to pump heat from low temperature to high temperature[20–26]. In analogy to stress transduction from a magnetostrictive material to a piezoelectric material (or vice versa) in multiferroic composites, there can be cooling mechanisms and devices based on multicaloric composite materials and structures. There is now a wide range of multiferroic materials with multiple order parameters that give rise to various novel physical phenomena and myriad applications[27–30]. Similarly, multicaloric cooling materials could lead to new ways of pumping heat.

This Review examines the physics of multicaloric cooling with respect to coupled ferroic order parameters in multiferroic materials. We first provide an overview of the development of monocaloric and multicaloric materials, before showing that all caloric cooling processes fall into one of four categories, depending on whether a material is a single phase or a composite and whether a single field or multiple fields are required for pumping heat. We then examine the scope of mechanocalorics and the different types of deformation modes, which provide diverse options for realizing multicaloric cooling. We also discuss how the dissipated percentage of input energy has a direct impact on the fatigue behaviour of multicaloric materials. In addressing these issues, we set the stage for examining whether multicaloric cooling helps improve the performance of caloric cooling technologies.

## Monocaloric and multicaloric effects

From a technological standpoint, the development of materials and devices often go hand in hand. In this section, we thus highlight key results from both caloric materials and devices. We start with a brief historical overview of the monocaloric materials used for magnetocaloric[9,31], electrocaloric[10,32] and mechanocaloric cooling[11,33,34], which serve as the basis of multicaloric cooling, before reviewing the development of multicalorics. For further information on monocaloric effects, we refer readers to REFS[3,35–39].

Either adiabatic temperature change ($\Delta T_{ad}$) or isothermal entropy change ($\Delta S$) can serve as the universal metric to quantify the caloric effect in materials. $\Delta T_{ad}$ directly correlates materials to systems (note that 'systems' refers to working devices and is used interchangeably with 'devices' herein): because $\Delta T_{ad}$ is the driving force for heat transfer between the solid refrigerant and the working fluid[40,41], this metric compares a materials property (experimentally measured $\Delta T_{ad}$) to the device performance (temperature span). $\Delta T_{ad}$ is also used to guide system design: if the $\Delta T_{ad}$ in the caloric materials is less than the required temperature span of the system, then methods such as cascading or active regeneration[42] are required to increase $\Delta T_{ad}$. $\Delta S$ is related to the amount of heat pumped in each cycle and has a material-specific relationship to $\Delta T_{ad}$. Herein, we use $\Delta T_{ad}$ as the metric to quantify the caloric effect.

The magnetocaloric effect, first discovered in 1917 by Weiss[43] in Ni, is observed when a magnetic field is applied to a magnetic material and then removed. When the field is applied, the magnetic moments align, leading to a decrease in entropy and release of heat into the surroundings (FIG. 1a). Removing the field results in undoing of the alignment, which causes an increase in entropy and absorption of heat from the surroundings (FIG. 1b). Magnetocaloric cooling was proposed in the mid-1920s, independently, by Debye[44] and Giauque[45], although the concept was not experimentally demonstrated until 1933 using paramagnetic salts[46]. Using this approach, Giauque and MacDougall[46] achieved temperatures close to 0 K, laying the foundation for the cryogenic technologies used today to reach ultralow temperatures. Indeed, Giauque received The Nobel Prize in Chemistry 1949 for his contribution "concerning the behaviour of substances at extremely low temperatures". In an important step towards achieving practical refrigeration at room temperature, in 1976, Brown first demonstrated that active magnetic regeneration near room temperature[47] could increase the natural $\Delta T_{ad}$ of Gd (14 K, with a magnetic field of 7 T) to the regenerator span of 47 K. Active regeneration has since been implemented in various caloric cooling devices to achieve large temperature spans. Giant magnetocaloric materials, Gd–Si–Ge alloys, that operate near room temperature were reported in 1997 (REF.[48]), followed by the discovery of La–Fe–Si alloys[49,50] and other rare-earth-free magnetocaloric materials, including Mn–Fe–P–Si (REF.[31]) and Ni–Mn-based alloys[9,51]. Several magnetocaloric cooling prototypes have been demonstrated, including a rotary-type cooler with a temperature span across the regenerator of 10.3 K at a cooling power of 288 W, a system coefficient of performance (COP) of 5.7 and a second-law efficiency (ratio of actual performance to the performance under ideal Carnot conditions) of 20.5%[52,53], as well as a rotary-type heat pump with a heating power of 340 W, a system COP of 6.7 and a second-law efficiency of 20.6% at a temperature span of 10.3 K (REF.[54]).

The electrocaloric effect is achieved by aligning electric dipoles using electric fields (FIG. 1c,d), in much the same way as the magnetic moments are aligned in magnetocaloric materials. In the first report of the electrocaloric effect, in 1930, Kobeko observed an electrocaloric temperature change in Rochelle salt (sodium potassium tartrate tetrahydrate)[55], for which Wiseman later reported a $\Delta T_{ad}$ of <4 mK at 295 K in 1963 (REF.[56]). In the 1960s, $\Delta T_{ad}$ values of <1 K were experimentally measured at cryogenic temperatures in $SrTiO_3$ (REFS[57,58]), $CdTiO_3$ (REF.[58]) and Li-doped KCl (REFS[59,60]). As a step towards room-temperature refrigeration, giant $\Delta S$ due to electric fields were indirectly measured in $Pb(Zr_{0.95}Ti_{0.05})O_3$ ceramic thin films above room temperature in 2006 (REF.[61]) and in ferroelectric polymer (poly(vinylidene fluoride-trifluoroethylene-chlorofluoroethylene)) thin films near room temperature in 2008 (REF.[32]). In pursuit of a large temperature lift, active regeneration was used to increase the $\Delta T_{ad}$ of 1.2 K in $0.9Pb(Mg_{1/3}Nb_{2/3})O_3$–$0.1PbTiO_3$ (PMN–10PT) bulk relaxor ceramics to a temperature span of 3.3 K in 2015 (REF.[15]). Marking an important milestone for electrocaloric materials and device design, multilayer capacitor configurations were used to achieve a $\Delta T_{ad}$ of 3.3 K over a temperature window of 73 K in 2019 (REF.[10]) and to demonstrate regenerative[62] and cascade[63] cooling in 2020. To enhance heat transfer through thermal contact, electrostatic actuation was used to move an electrocaloric polymer film between a heat source and a heat sink in 2017 (REF.[64]), and this approach was subsequently applied in cascade cooling in 2020 (REF.[65]).

The mechanocaloric effect has primarily been studied in two mechanical-force configurations. One is the elastocaloric effect (FIG. 1e,f), which is most commonly observed as the temperature change of Indian rubber when it is stretched and released[66]. In the first systematic study on the phenomena related to the elastocaloric effect, in 1859, Joule reported the temperature changes (0.01–1.5 K) exhibited by a series of materials, including steel, copper, lead, glass and wood, under uniaxial stress (tension and compression)[67]. The word 'elastocaloric' first appeared in 1962, referring to the response of a Ge single crystal at a low temperature of 1 K (REF.[68]). Working towards the effect near room temperature, the elastocaloric effect has more recently been primarily studied in superelastic shape-memory alloys, including Cu–Al–Ni, Cu–Zn–Al, Ni–Ti and Ti–Ni–Cu (REFS[33,34,69–71]). Some of the largest caloric effects among monocaloric materials in terms of $\Delta T_{ad}$ and $\Delta S$ have been observed in elastocaloric materials[72–74]. As an example, the latent heat of martensitic transformations in shape-memory alloys can be as large as 35.1 J g$^{-1}$ (REF.[75]), and, at a specific heat capacity of 0.4 J kg$^{-1}$ K$^{-1}$ in $Ni_{49.8}Ti_{30.2}Hf_{20}$, this translates to a $\Delta T_{ad}$ of up to 87.8 K, which is a theoretical upper limit in this case (in practice, experimentally observed values are lower, owing to losses). Working

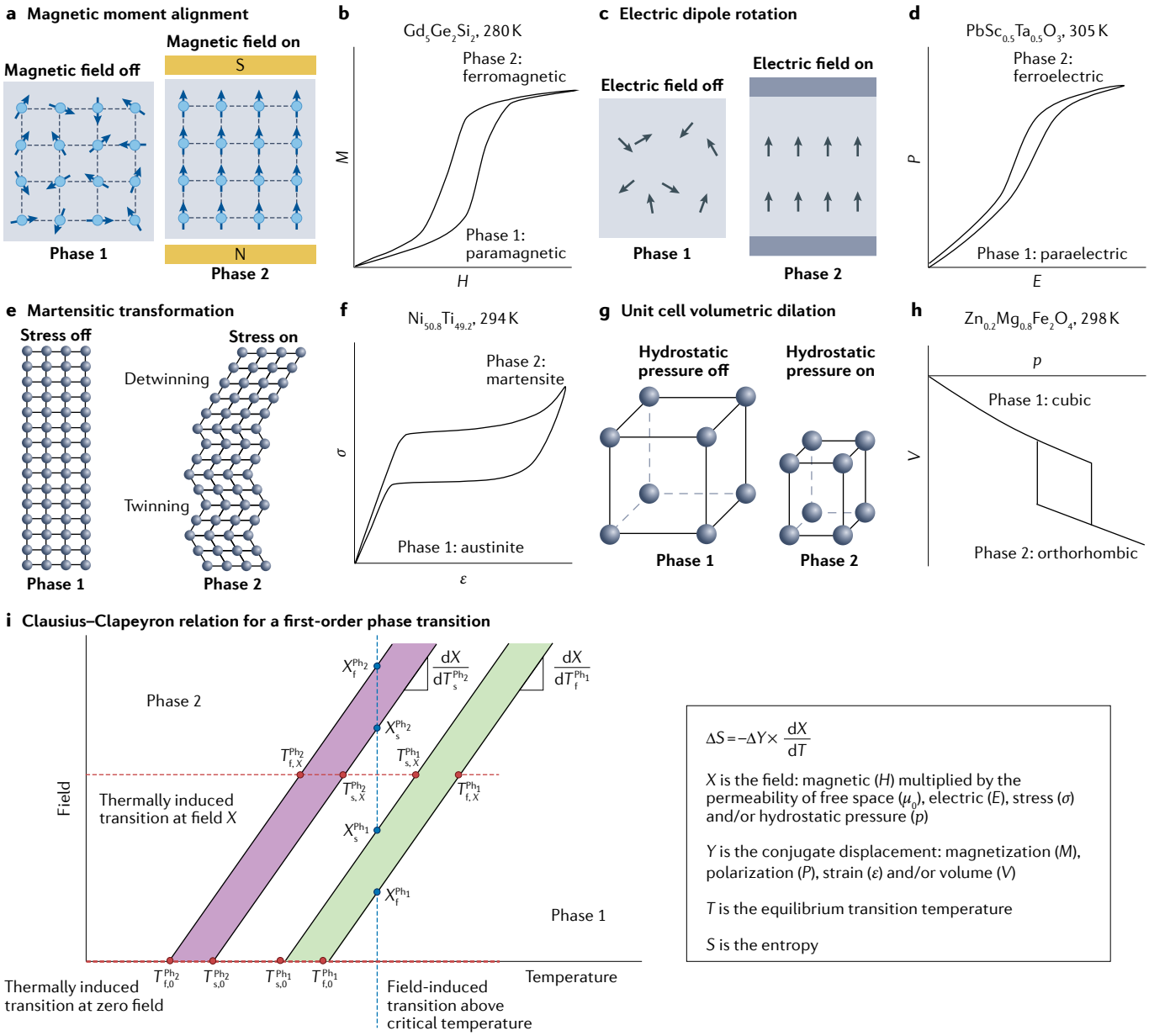


Fig. 1 | **Mechanisms of monocaloric materials as the basis for multicaloric cooling. a**,**b** | The magnetic moments switch between aligned and disordered states upon turning the magnetic field on and off (panel **a**), as manifested in the magnetization (*M*) versus applied magnetic field (*H*) curve at a paramagnetic–ferromagnetic transition (panel **b**). **c**,**d** | The electric dipolar states change between aligned and randomized upon turning the electric field on and off (panel **c**), as seen in the polarization (*P*) versus applied electric field (*E*) curve at a paraelectric–ferroelectric transition (panel **d**). **e**,**f** | The crystal structure transforms between a high-symmetry and a twinned-then-detwinned structure as stress is applied and released (panel **e**), which is seen in the applied stress ($\sigma$) versus strain ($\varepsilon$) curve at an austinite–martensite transition (panel **f**). **g**,**h** | The unit cell volume dilates and is then restored — accompanied by a change in the lattice parameter — when hydrostatic pressure is applied and removed (panel **g**), as displayed in the volume (*V*) versus applied hydrostatic pressure (*p*) curve at a pressure-induced cubic–orthorhombic transition (panel **h**). The curves in panels **b**, **d**, **f** and **h** are for representative materials at typical test temperatures. The rotating localized magnetic and electric dipoles in panels **a** and **c** represent just one of the modes of caloric cooling effects involving magnetic and electric fields, respectively, and were selected for illustrative purposes. **i** | The Clausius–Clapeyron relation for a first-order phase transition. The high-temperature, low-field stabilized phase, phase 1 ($Ph_1$), typically possesses a high-symmetry structure, such as cubic, and the low-temperature, high-field stabilized phase, phase 2 ($Ph_2$), has a low-symmetry structure. The $Ph_1 \leftrightarrow Ph_2$ transition can be either field induced at a temperature higher than the transition temperatures, thermally induced at zero field or thermally induced at a finite field with shifted transition temperatures. For a field-induced transition, $X_s^{Ph_1}$, $X_f^{Ph_1}$, $X_s^{Ph_2}$ and $X_f^{Ph_2}$ (where the field *X* can be *H*, *E*, $\sigma$ or *p*) are the fields at which different phases appear at the transition (the subscripts 's' and 'f' denote the start and finish points, respectively). $T_{s,0}^{Ph_1}$, $T_{f,0}^{Ph_1}$, $T_{s,0}^{Ph_2}$ and $T_{f,0}^{Ph_2}$ are the temperatures at which different phases appear under zero field (denoted by subscript '0'), whereas $T_{s,X}^{Ph_1}$, $T_{f,X}^{Ph_1}$, $T_{s,X}^{Ph_2}$ and $T_{f,X}^{Ph_2}$ are the temperatures at which different phases appear under finite field (denoted by the subscript '*X*'). The slope of the phase boundaries, $\frac{dX}{dT_f^{Ph_1}}$ and $\frac{dX}{dT_s^{Ph_2}}$, above the critical temperatures can be experimentally determined and equal $\frac{dX}{dT}$ in the Clausius–Clapeyron relation. $\frac{dX}{dT}$ can be used to calculate the entropy change through the equation shown on the right. Panel **b** adapted from REF.[142], Springer Nature Limited. Panel **d** adapted from REF.[255], CC BY 4.0. Panel **f** adapted with permission from REF.[11]. © The Authors, some rights reserved; exclusive licensee AAAS. Panel **h** adapted with permission from REF.[301], American Physical Society.

towards a commercial cooling technology, the first elastocaloric cooling prototype device was demonstrated in 2012, with Ni–Ti wires in a tension mode in a rotating bird-case-like configuration[76]. More recent advances in elastocaloric systems include a compression-based cooling device with heat recovery[77] and the demonstration of a regenerative elastocaloric heat pump[14].

The other main mechanocaloric cooling mode is based on the barocaloric effect (FIG. 1g,h), whereby an entropy change is observed in a material upon application of hydrostatic pressure, which causes a volume change in the unit cell that is often accompanied by lattice distortion. As an early study, in 1982, a $\Delta T_{ad}$ of up to 9 K was experimentally measured in poly(methyl methacrylate)[78] under a pressure of 200 MPa at 643 K. $\Delta T_{ad}$ values of 2 K were measured for the inorganic rare-earth compounds $Pr_{0.66}La_{0.34}NiO_3$ (at 300 K and 1,500 MPa)[79] and CeSb (at 21 K and 520 MPa)[80] in 1998 and 2000, respectively. In pursuit of a large barocaloric effect, a $\Delta S$ per mass of 27.0 J kg$^{-1}$ K$^{-1}$ was indirectly measured near room temperature in Ni–Mn–In alloys at 260 MPa in 2010 (REF.[17]), and values of 22.3 J kg$^{-1}$ K$^{-1}$ in Mn–Ga–N alloys at 139 MPa (REF.[81]) and 60.0 J kg$^{-1}$ K$^{-1}$ in inorganic salts at 100 MPa (REF.[82]) in 2015. More recently, the barocaloric effect has also been indirectly measured in perovskite-structure compounds[83,84], superionic conductors[85], plastic crystals (both the reversible endothermic and exothermic processes are reported in REFS[86–88], whereas the exothermic process only is reported in REF.[89]) and spin-crossover compounds[12,90–92].

The parallel development of monocaloric effects has converged to the focus point of multicaloric effects. An early development in this area was the observation in 1996 of different types of monocaloric effects in the same material: an elastocaloric $\Delta T_{ad}$ of 5.2 K by varying the tensile uniaxial stress by 529 MPa and a magnetocaloric $\Delta T_{ad}$ of 8.3 K by varying the magnetic field by 2.5 T were separately measured in Fe–Rh alloy using a direct method[26]. Subsequent developments in the 2000s mostly used hydrostatic pressure as a constant field to influence the magnetocaloric effect in various materials, namely, to enhance the magnitude of the entropy change in MnAs (REF.[93]), modify the order of the transition in $Tb_5Si_2Ge_2$ (REF.[94]), tune the transition temperatures in $Gd_5Si_2Ge_2$ (REF.[95]) and shift the operating temperature window in La(Fe,Si)$_{13}$-type compounds[96] and Heusler-type alloys[9]. Theoretical work in 2007 predicted that the operating temperature windows of $ErCo_2$ could be widened by simultaneously varying a magnetic field by 4 T and the pressure by 1.5 GPa at ~30 K (REF.[97]). It was not until 2010 that the term 'multicaloric' first appeared in the literature[17]. Since then, the volume of research on multicaloric effects has substantially increased: theories have been proposed[23,98], different types and combinations of external fields have been experimentally demonstrated and different types of materials that are responsive to more than one external field have been explored. To date, there are three reported types of multicaloric operation: multiple external fields are varied simultaneously, one external field is varied while the other external fields are held at a non-zero value or one external field is varied while the others are zero (see Supplementary Table 1 for a comprehensive list of examples, materials and references).

Not only have the types of multicaloric materials diversified but also the configurations, which have expanded from single-phase materials to composite materials, wherein the constituents respond to different types of external field. One configuration is a thin film deposited on a substrate; in this composite, the caloric thin film is subjected to one external field and the substrate to another as a tuning parameter in a multicaloric cooling cycle[99–101]. Another configuration is to subject a composite material to a single external field that is transduced into another type of field by one constituent of the composite to act on the other constituent. In an early report of this approach, strain transduction was exploited in $La_{0.7}Ca_{0.3}MnO_3$ films deposited on $BaTiO_3$ substrates to generate a giant magnetocaloric effect[102]; an applied magnetic field generates a magnetostrictive strain in the film that drives a first-order structural phase transition in the substrate, which, in turn, increases the magnetization and entropy changes in the film. In another early example, magneto-elastocaloric cooling was demonstrated using a composite comprising $Tb_xDy_{1-x}Fe_2$ ($x \approx 0.3$, Terfenol-D) and Cu–Al–Mn (REF.[103]). Under an external magnetic field, the transduction component — Terfenol-D — transduces the applied field into a mechanical field, which is used to drive the heat-pump cycle (or refrigeration cycle) in the elastocaloric component, Cu–Al–Mn.

In multicaloric effects, we consider multiple (and, sometimes, coupled) responses of materials to various fields, stemming from the coexistence of magnetic, polar and structural degrees of freedom associated with phase transitions. The thermodynamics of the caloric effects associated with first-order phase transitions are well captured by the Clausius–Clapeyron relation, which describes the field-induced $\Delta S$ at a full or partial transition[33,98,104]. The phase diagram in FIG. 1i shows the hysteresis of the first-order transition in a material between a high-temperature, low-field stabilized phase (phase 1 ($Ph_1$)) and a low-temperature, high-field stabilized phase (phase 2 ($Ph_2$)). There are four distinct corresponding temperatures at zero field ($T_{s,0}^{Ph_1}$, $T_{f,0}^{Ph_1}$, $T_{s,0}^{Ph_2}$, $T_{f,0}^{Ph_2}$) and at a finite field ($T_{s,X}^{Ph_1}$, $T_{f,X}^{Ph_1}$, $T_{s,X}^{Ph_2}$, $T_{f,X}^{Ph_2}$), and four critical field values at a constant temperature ($X_s^{Ph_1}$, $X_f^{Ph_1}$, $X_s^{Ph_2}$, $X_f^{Ph_2}$), where the subscripts 's' and 'f' indicate the start and finish of the phase transition, respectively, and '0' and '$X$' denote a zero and non-zero field, respectively. At each of these points, there is a sharp change in a ferroic property during the transition. $X$ can be a magnetic field, electric field, stress field, hydrostatic pressure or a combination thereof. The slope of the phase boundaries, $\frac{dX}{dT}$, is a measure of the sensitivity of the critical transformation field to temperature and connects the ferroic properties to the entropy changes in indirect measurements of caloric effects[3]. The phase diagram in a field–temperature space thus establishes a roadmap for the first-order phase transitions associated with caloric effects. In the case of multicaloric effects, a combination of fields, such as $X_1$ and $X_2$, can be applied simultaneously or sequentially, and the resultant response can be 'separate' ($\Delta S(X_1) + \Delta S(X_2)$) or 'cooperative' ($\Delta S(X_1, X_2)$).

## Taxonomy of multicaloric cooling

Given the diversity of materials that exhibit multiple ferroic order parameters, there have been many reports of different types of multicaloric cooling. There have also been numerous reports of multicaloric composites in which interfacial coupling through transduced stress between the constituents is used as a primary or secondary field to pump heat. By considering the different combinations of external fields and materials, we have classified caloric cooling processes into four major categories (FIG. 2a), depending on whether a material is single phase or composite (FIG. 2b,c) and whether a single or multiple fields are applied for heat pumping (FIG. 2d). In this context, we define multicaloric materials as single-phase or composite materials that possess at least one type of ferroic order (such as lattice, magnetic or ferroelectric) and display a caloric effect in response to more than one type of external field. When the signs of the field-induced caloric effect due to more than one external field are different in a multicaloric material, judicious design of the multicaloric operation is necessary to attain additive instead of subtractive effects. In general, the magnitude of the caloric effect for a given field varies with the magnitude of the field in a given direction. The absolute value of the caloric effect increases with the increasing magnitude of the field that is varied until saturation. Normally, driving a caloric effect by increasing a unipolar field or 'undriving' by decreasing the field does not affect this proportionality. Below, we describe each of the four caloric cooling categories and give examples of materials. Additional materials, together with the directionality of the applied fields and the signs of the field-induced caloric effects, are detailed in Supplementary Table 1.

***Single field on single-phase materials.*** According to our categorization, the first class of caloric cooling mode is based on the application of a single field to a single-phase material (quadrant I in FIG. 2a). This mode encompasses the monocaloric effects, namely, the magnetocaloric, electrocaloric and mechanocaloric (including elastocaloric and barocaloric) effects discussed above (I.1–I.3 in FIG. 2d).

***Multiple fields on single-phase materials.*** Because multiferroic and multicaloric materials can respond to multiple fields (the overlap regions in FIG. 2b), the first type of multicaloric cooling is the application of multiple fields to single-phase materials (quadrant II in FIG. 2a and II.1–II.4 in FIG. 2d). The overlap region II.1 in FIG. 2b represents single-phase materials in which cooling can be induced with either a magnetic field and/or a stress field (II.1 in FIG. 2d). For example, $Gd_5(Si_xGe_{1-x})_4$ alloys with $0.24 \leq x \leq 0.5$ exhibit a first-order magnetic transition from a paramagnetic to a ferromagnetic phase upon cooling, while the corresponding structures undergo a transition from a high-temperature monoclinic to a low-temperature orthorhombic phase[105,106]. Thus, the total transition entropy change comprises the entropy change from the structural degree of freedom and the magnetic-field-induced entropy change, which add with the same sign. A moderate hydrostatic pressure of 200 MPa can induce a magneto-structural transition in $Gd_5Si_2Ge_2$ that gives rise to an entropy change comparable with that induced by the magnetic field only[107]. Another family of materials in this category is Heusler Ni–Mn–$Z$ ($Z$ = In (REFS[108,109]), Ga (REF.[110]) and Sn(Cu) (REF.[111]) alloys. As the structural transition temperature is close to the Curie temperature in these materials, and the temperature ranges over which the material exhibits different kinds of ferroic order must also overlap, elastocaloric and magnetocaloric effects simultaneously emerge. In these Heusler alloys, an increase in entropy and a decrease in temperature can be achieved by applying a magnetic field, known as the inverse magnetocaloric effect, or by removing a uniaxial stress field, which is the conventional elastocaloric effect. For $Ni_{50}Mn_{35.5}In_{14.5}$, by properly combining a uniaxial stress field of 40 MPa and a magnetic field of 4 T to add the caloric effects cooperatively, its caloric response in terms of $\Delta S$ can be increased from 9.5 to 14 J kg$^{-1}$ K$^{-1}$, which is an increase of 47% compared with its response to a single stimulus[108].

The overlap region II.2 in FIG. 2b corresponds to single-phase materials in which cooling can be induced by electric and/or uniaxial stress fields[112,113] (II.2 in FIG. 2d). An example of such a material is the correlated oxide $VO_2$. During the famous metal–insulator transition in $VO_2$, the crystal symmetry changes from a tetragonal (rutile) structure in the metallic state to a monoclinic structure and is accompanied by a latent heat as large as 51.5 J g$^{-1}$ (REF.[114]). Using a relatively low electric field of $7.5 \times 10^{-3}$ MV m$^{-1}$, a $\Delta S$ of 94 J kg$^{-1}$ K$^{-1}$ was achieved in a 0.4-mm-thick $VO_2$ pellet[112], whereas exerting a uniaxial stress field of 300 MPa on $VO_2$ powders that were pressed into a pellet with a diameter of 6 mm resulted in a $\Delta T_{ad}$ of 1.6 K (REF.[113]). The materials in region II.3 of FIG. 2b exhibit cooling upon application of a magnetic and/or electric field (II.3 in FIG. 2d). For example, the application of an electric field of 15 MV m$^{-1}$ to $Pb(Fe_{0.5}Nb_{0.5})O_3$–$BiFeO_3$-based ceramics[115] leads to a directly measured $\Delta T_{ad}$ of 1.5 K at room temperature and 1.8 K at 348 K, whereas a magnetic field of 9 T produced an indirectly measured $\Delta T_{ad}$ of 0.3 K at 3 K. To the best of our knowledge, there has not been an experimentally reported demonstration of a single-phase material that exhibits a caloric response to electric, magnetic and stress fields (II.4 in FIG. 2b,d). However, simulations have shown that the simultaneous application of electric, magnetic and stress fields to $BiFeO_3$ could give rise to a $\Delta T_{ad}$ of 12 K (REF.[116]). Similarly, it was predicted that applying an electric field of 10 MV m$^{-1}$ at a constant pressure of 200 MPa to epitaxial $EuTiO_3$ thin films[117] results in a $\Delta T_{ad}$ of 5.31 K and that applying a magnetic field of 5 T alone leads to a $\Delta T_{ad}$ of 17.3 K.

***Single field on composite materials.*** The next type of multicaloric cooling is the application of a single field to a composite configuration (quadrant III in FIG. 2a), in which one component in the composite transduces the field needed to pump heat in the other (the caloric component). Given the diversity of transduction (and multiferroic) materials, the transduced field (due to the conjugate displacements) can be a magnetic field (due to magnetization), a stress field (due to strain at interfaces) or an

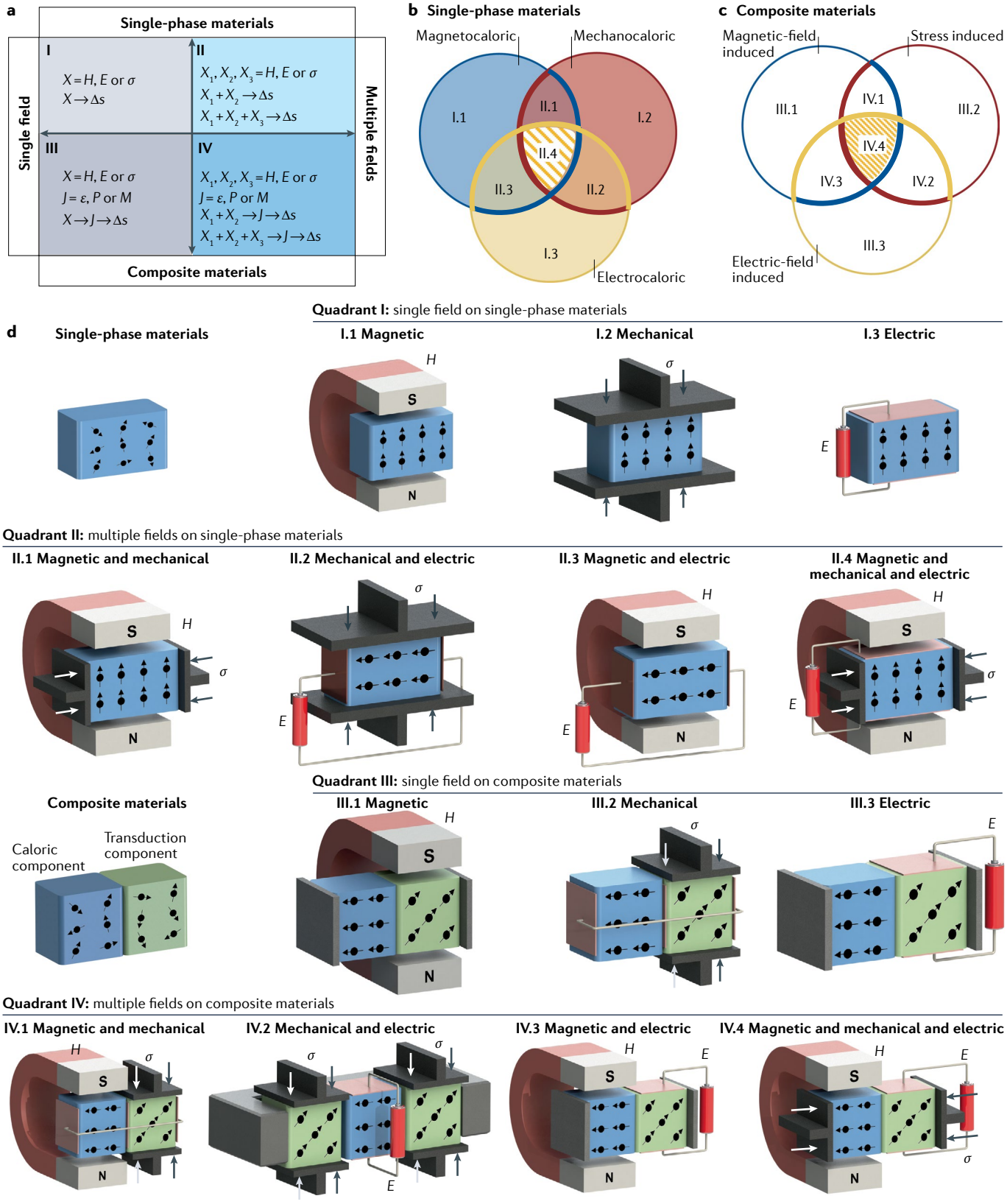


electric field (due to accumulated charges or polarization) (III.1–III.3 in FIG. 2c,d). However, we expect the most prevalent transduction mode to be stress. One demonstrated example is magneto-elastocaloric cooling (III.1 in FIG. 2d). In this study, a magnetostrictive material, Terfenol-D, was placed in contact with an elastocaloric Cu–Al–Mn alloy[103]. An ultralow magnetic field of 0.16 T induced a $\Delta T_{ad}$ of up to 4 K in the device, representing a multifold increase in the magnetic-field cooling strength (defined as $\Delta T_{ad}$/applied field) compared with that of 'pure' magnetocaloric cooling

◀ Fig. 2 | **Categories of caloric cooling. a** | All monocaloric and multicaloric materials and configurations can be categorized into four quadrants (I–IV) based on whether the materials are single phase or composite and whether single or multiple fields are applied. $X_n$ ($n = 1–3$) represents different applied fields (magnetic ($H$), electric ($E$) or stress ($\sigma$)). Multicaloric effects in composite materials typically involve the indirect transfer of a conjugate displacement ($J$), which is typically strain ($\varepsilon$) but, in certain cases, can be magnetization ($M$) or polarization ($P$). $\Delta s$ denotes the specific entropy change. In configurations with multiple fields, the fields can be applied simultaneously (for example, $X_1$ and $X_2$) or sequentially (for example, $X_1$ first and then $X_2$). **b** | Venn diagram illustrating the relationship between magnetocaloric, mechanocaloric, electrocaloric and multicaloric cooling processes in single-phase materials. **c** | Venn diagram illustrating the relationship between magnetic-field-induced, stress-induced and electric-field-induced processes, as well as combinations thereof, in composite materials. **d** | Configurations of single-phase materials under a single applied field (I.1–I.3), single-phase materials under multiple fields (II.1–II.4), composite materials under a single field (III.1–III.3) and composite materials under multiple fields (IV.1–IV.4). The ferroic order parameters within materials are denoted by arrows with black circles and denote the state of any one of the ferroic order parameters ($\varepsilon$, $M$ or $P$). For quadrant IV, the composites shown in the figure are laminates, but other configurations involving bulk composites or epitaxial multilayers are also possible. See Supplementary Fig. 2 and Supplementary Note 1 for additional configurations of composite materials. The magnetic field can be varied by changing the electric current for electromagnets and superconducting magnets at static positions or by moving permanent magnets with respect to the materials. The directionality of the different fields in each case represents one of the possibilities.

(I.1 in FIG. 2d). This composite effect can mitigate the large fields typically required for single-phase, single-field caloric cooling. As only one component in the composite undergoes cooling in a limited volume, this effect could be implemented in specialized applications such as remote localized cooling of electronic devices[118]. A straightforward extension of the magneto-elastocaloric cooling design would be an electro-elastocaloric effect (III.3 in FIG. 2d), whereby piezo-induced strain is used to apply stress to the elastocaloric material[103]. Another variation is a mechano-magnetocaloric effect (III.2 in FIG. 2d). In this case, the application of stress to a magnetostrictive material leads to alignment of the magnetization, which is used as the source of a magnetic field for a magnetocaloric material placed in contact. Note that if the caloric component in a composite multicaloric exchanges heat with the transduction component, a heat-insulating and mechanically stiff object, such as a ceramic disc[103], should be inserted between the caloric and transduction components.

***Multiple fields on composite materials.*** The final category of multicaloric cooling is the application of multiple fields to composite materials (quadrant IV in FIG. 2a and IV.1–IV.4 in FIG. 2c,d). There have been several demonstrations of magnetocaloric Fe–Rh thin films coupled elastically to piezoelectric substrates (IV.3 in FIG. 2d). In a $Fe_{50}Rh_{50}/BaTiO_3$ composite, there was an apparent 96% reduction in hysteretic losses in the dual stimulus loops of a magnetocaloric Fe–Rh film through strain-mediated coupling with the substrate in a multistep cycle[99]; however, the dissipated energy associated with the hysteresis was transferred from the magnetic cycle to the elastic cycle. In $Fe_{50}Rh_{50}$/PMN–30PT composites to which an electric field was applied to (001)-oriented or (011)-oriented single crystals of PMN–30PT, the Fe–Rh film underwent a phase transition that is influenced by the domain switching in the PMN–30PT substrate. As a result, the magnetic-field-induced $\Delta S$ and refrigeration capacity[101], as well as the operating temperature window of the magnetocaloric effect in the Fe–Rh film[100], notably improved, in addition to a reduction in hysteresis. By applying an electric field of $125 \times 10^{-3}$ MV m$^{-1}$ (REF.[119]), a bilayer composite of 0.2-mm-thick $Fe_{48}Rh_{52}$ and 0.2-mm-thick $Pb(Zr_{0.53}Ti_{0.47})O_3$ in a varying magnetic field of 0.62 T displayed a 2.7-K increase in the transformation temperature for the magnetic phase transition in Fe–Rh. Moreover, there was a 33% reduction in thermal hysteresis, from 4.5 K to 3 K, although the dissipated energy associated with the hysteresis was transferred. In another example, a composite comprising 12 wt% magnetocaloric and magnetostrictive $Gd_5Si_{2.4}Ge_{1.6}$ microparticles embedded in a piezoelectric and pyroelectric poly(vinylidene) fluoride matrix exhibited a smaller $\Delta S$ of 2.3 J kg$^{-1}$ K$^{-1}$ under application of a magnetic field of 5 T at 265 K compared with a $\Delta S$ of 2.6 J kg$^{-1}$ K$^{-1}$ in pure $Gd_5Si_{2.4}Ge_{1.6}$ microparticles[120]. The difference in $\Delta S$ is due to the interaction of $Gd_5Si_{2.4}Ge_{1.6}$ with the poly(vinylidene) fluoride matrix through magnetoelectric coupling, indicating that the use of an additional electric field on the composite might provide another knob to tune the multicaloric effect. To the best of our knowledge, there have not been theoretical or experimental reports of the multicaloric configurations corresponding to regions IV.1, IV.2 or IV.4 in FIG. 2b,d, but we expect that such configurations will be reported in the near future. As a straightforward embodiment, for the above-mentioned Terfenol-D/Cu–Al–Mn alloy composite magneto-elastocaloric configuration, one could apply both a magnetic field (to the Terfenol-D component) and stress (to the elastocaloric component) to enhance the multicaloric effect.

Although the choice of pairing piezoelectricity, piezomagnetism, electrostriction, magnetostriction or other effects[27] by combining multiple external fields provides a rich playground for exploring multicaloric cooling, the construction of caloric devices that require multiple fields might be limited by their thermodynamic performance and the complexity and cost of system integration. However, multicaloric cooling devices might provide niche solutions for specialized applications, such as when one is able to reduce the necessary magnitude of an expensive field by applying another field. For example, a caloric effect driven by the magnetic field from an expensive permanent magnet configuration with no mechanical field could be equivalently driven by a combination of the magnetic field from an inexpensive permanent magnet configuration and a mechanical field from a relatively inexpensive, off-the-shelf mechanical actuator[121]. Another specialized application is when it is necessary to expand the operating temperature window of a device by applying multiple fields.

## Mechanocalorics as the basis for multicalorics

Stress transduction and/or mechanocaloric effects often have an important role in multicaloric cooling configurations. We, therefore, examine mechanocaloric modes in more detail in this section. The mechanocaloric effect has been primarily demonstrated in magnetic and non-magnetic shape-memory alloys[37,122,123], although there have also been reports for other types

of materials, including polymers[124–126] and ceramics[127,128]. Mechanocaloric materials typically exhibit mechanical properties that favour deformation under the application of stress. Non-magnetic shape-memory alloys such as Ni–Ti are ductile, whereas magnetic shape-memory alloys such as Ni–Mn–Ga are more brittle, which poses challenges for obtaining large deformations to achieve a sizable mechanocaloric effect. The underlying mechanism of the shape-memory effect is a diffusionless martensitic phase transformation. The shape deformation that accompanies a martensitic transformation in an unconstrained single crystal has the well-known characteristics of the invariant-plane strain, for which there exists an unrotated and undistorted plane that adjoins the transformed and untransformed phases[129]. Invariant-plane strains manifest in three forms: dilatational strain (responsible for the volume change of a crystal), shear strain (responsible for the shape change of a crystal) and their combination. When a lattice transformation from a parent crystal to a product crystal requires an invariant-line (unrotated and undistorted) strain, such as the transformation from body-centred cubic to face-centred cubic[130], the invariant-plane strain experimentally observed as a macroscopic shape change needs to be intersected by a second invariant-plane strain that is made macroscopically invisible by lattice invariant shear through slip or twinning[131].

From a mechanics point of view, dilation of an infinitesimal volume element at a point in a solid material results from the application of isotropic stress, namely, hydrostatic pressure, whereas shear strain can be generated by resolving applied stress into shear stress along a projected direction. Application of isotropic stress (hydrostatic pressure) leads to dilatational strain and an entropy change that results in a barocaloric effect, whereas shear strain from uniaxial stress can lead to an entropy change during the transformation that results in an elastocaloric effect. To date, most applied stresses in reported elastocaloric effects are uniaxial, either tensile or compressive, probably owing to the fact that uniaxial stress is the simplest example of deviatoric stress that can be applied in laboratory testing.

Deviatoric stress represents a departure in a stress state from hydrostatic pressure, and, in addition to uniaxial stress, there can be numerous stress states. The different elemental types of deviatoric stress and the corresponding mechanocaloric effects are defined in BOX 1. We use the term 'deviatocaloric' to collectively describe the caloric effects associated with deviatoric stresses. The elastocaloric effect based on uniaxial stress is just one of the types of deviatocaloric effect. In fact, any stress state in a solid body can be decomposed into hydrostatic and deviatoric stress components. Thus, barocaloric and deviatocaloric effects together make up the family of mechanocaloric effects (BOX 1). Recently, there have also been reports of large caloric effects achieved using different deviatoric stresses, including torsional stress[132,133] and bending stress[134–137]. In the case of torsional stress, $\Delta T_{ad}$ values of up to 20.8 K have been observed[132], whereas bending stress has produced $\Delta T_{ad}$ values as large as 15.4 K. Given that these reports with large caloric effects have appeared only in the past 3 years, it is likely that other deviatoric effects are being explored or will be reported soon. Demonstration of hitherto unexplored deviatocaloric modes might also lead to the development of new materials.

Because internal stress states of materials are often intimately coupled to other properties, such as local magnetic ordering and electric dipole moments, materials that exhibit field-induced properties are likely to also display deviatocaloric effects owing to multicaloric coupling. One good example is a ferroelectric material that exhibits a flexoelectric effect, which can produce a flexocaloric response[138]. Another example is the recently reported presence of nematic fluctuations in Fe-based superconductors, which display an elastocaloric effect[139,140].

## Hysteresis versus durability

Hysteresis in the space of the field–conjugate displacement (FIG. 1i) has been widely recognized as the key parameter that governs the durability and fatigue life of caloric materials[6,11,37,141–144]. For many materials, the hysteresis is a direct measure of the efficiency of the first-order transition associated with the caloric effect and is a simple yet quantifiable parameter used to assess the performance of cooling cycles and devices[145–148]. In first-order phase transitions, hysteresis represents the energy that is dissipated during a change in ferroic order parameters through dissipative losses of various origins, such as internal friction[149,150] or domain-wall pinning[151–154]. The conventional wisdom[152,155–158] is that a phase-transforming material with small hysteresis will degrade less and, thus, last longer than a material with large hysteresis. Mechanical integrity is crucial to all caloric materials and their applications, particularly mechanocaloric materials. For electrocaloric cooling, the breakdown of electrical insulation (which might be accompanied by mechanical breakdown) is a major cause of failure and degradation. For magnetocaloric materials, aside from corrosion due to contact with the heat-exchange medium[159,160], mechanical brittleness[161], as well as fatigue and mechanical breakdown due to magnetostriction[3,143], have been reported. Thus, mechanical properties and integrity have various roles in governing the degradation behaviour of different types of caloric materials. As such, reducing (and, ideally, eliminating) hysteresis has been a central goal in the caloric materials community, and various strategies to minimize hysteresis have been proposed (see the table within BOX 2 and Supplementary Table 7). One well-accepted strategy is to tune the composition of the materials in order to optimize lattice compatibility and reduce mismatch strains between phases[141,162], thereby, minimizing the formation of interfacial defects during transformation and, thus, extending the lifetime.

Multicaloric materials with coexisting (and, sometimes, coupled) order parameters have unique energy landscapes, in which different field–variable pairs (FIG. 1i) create dissipative energy losses. The energy transfer associated with the reduction of hysteresis from one field–variable pair to another can have profound implications on the overall energy landscapes (see Supplementary Note 2 and Eq. S11 for a discussion on energy transfer). In addition to the intrinsic hysteresis of the materials,

Box 1 | **Mechanocaloric processes**

Many of the multicaloric cooling configurations involving composite materials (FIG. 2) use mechanical transduction. The most common mechanocaloric effects are the elastocaloric (by uniaxial stress) and the barocaloric (by isotropic stress) effects. The elastocaloric effect belongs to a family known as 'deviatocaloric' effects (see the figure), which reflect various forms of deformation and stress distribution. Four other elemental types of deviatocaloric effects are twistocaloric (by torsional stress), flexocaloric (by bending stress), shearocaloric (by shear stress) and hollocaloric (by plane stress).

In general, the stress state of a point in a solid body is expressed in tensor notation as

$$\sigma_{ij} = \begin{bmatrix} \sigma_{xx} & \sigma_{xy} & \sigma_{xz} \\ \sigma_{xy} & \sigma_{yy} & \sigma_{yz} \\ \sigma_{xz} & \sigma_{yz} & \sigma_{zz} \end{bmatrix}$$

where the subscripts denote normal stress if they are the same, otherwise, they denote shear stress in a rectangular coordinate system *xyz*. The stress state can be decomposed as $\sigma_{ij} = \breve{\sigma}_s + \tilde{\sigma}_d$, where $\breve{\sigma}_s$ is a spherical stress tensor,

$$\breve{\sigma}_s = \begin{bmatrix} \sigma_m & 0 & 0 \\ 0 & \sigma_m & 0 \\ 0 & 0 & \sigma_m \end{bmatrix}, \text{ where } \sigma_m = \frac{1}{3}(\sigma_{xx} + \sigma_{yy} + \sigma_{zz})$$

and $\tilde{\sigma}_d$ is a deviatoric stress tensor:

$$\tilde{\sigma}_d = \begin{bmatrix} \sigma_{xx} - \sigma_m & \sigma_{xy} & \sigma_{xz} \\ \sigma_{xy} & \sigma_{yy} - \sigma_m & \sigma_{yz} \\ \sigma_{xz} & \sigma_{yz} & \sigma_{zz} - \sigma_m \end{bmatrix}$$

$\breve{\sigma}_s$ is a hydrostatic state and is responsible for isotropic, volumetric deformation, whereas $\tilde{\sigma}_d$ measures deviation from the hydrostatic state and causes shape changes. The barocaloric effect corresponds exclusively to $\breve{\sigma}_s$, whereas the elastocaloric process is one scenario of $\tilde{\sigma}_d$; $\tilde{\sigma}_d$ produces other elemental processes and many combined processes. The deformation mode, the resulting stress distribution on the cross section and infinitesimal cube-shaped volume element, and the corresponding stress tensor of the barocaloric effect and five elemental deviatocaloric effects are shown in the figure. The formulae to compute stress from internal loading are in Supplementary Table 2.

Caloric effects can be achieved through complex deformation modes by combining different types of mechanocaloric effect. For example, elasto-twistocalorics can be realized by combining elastocalorics and twistocalorics through the application of a set of uniaxial force and torsional moment.

$\sigma$, normal stress; $\tau$, shear stress; $F_n$, normal force; $F_s$, shear force; $M_b$, bending moment; $M_t$, torsional moment; $p$, gauge pressure.

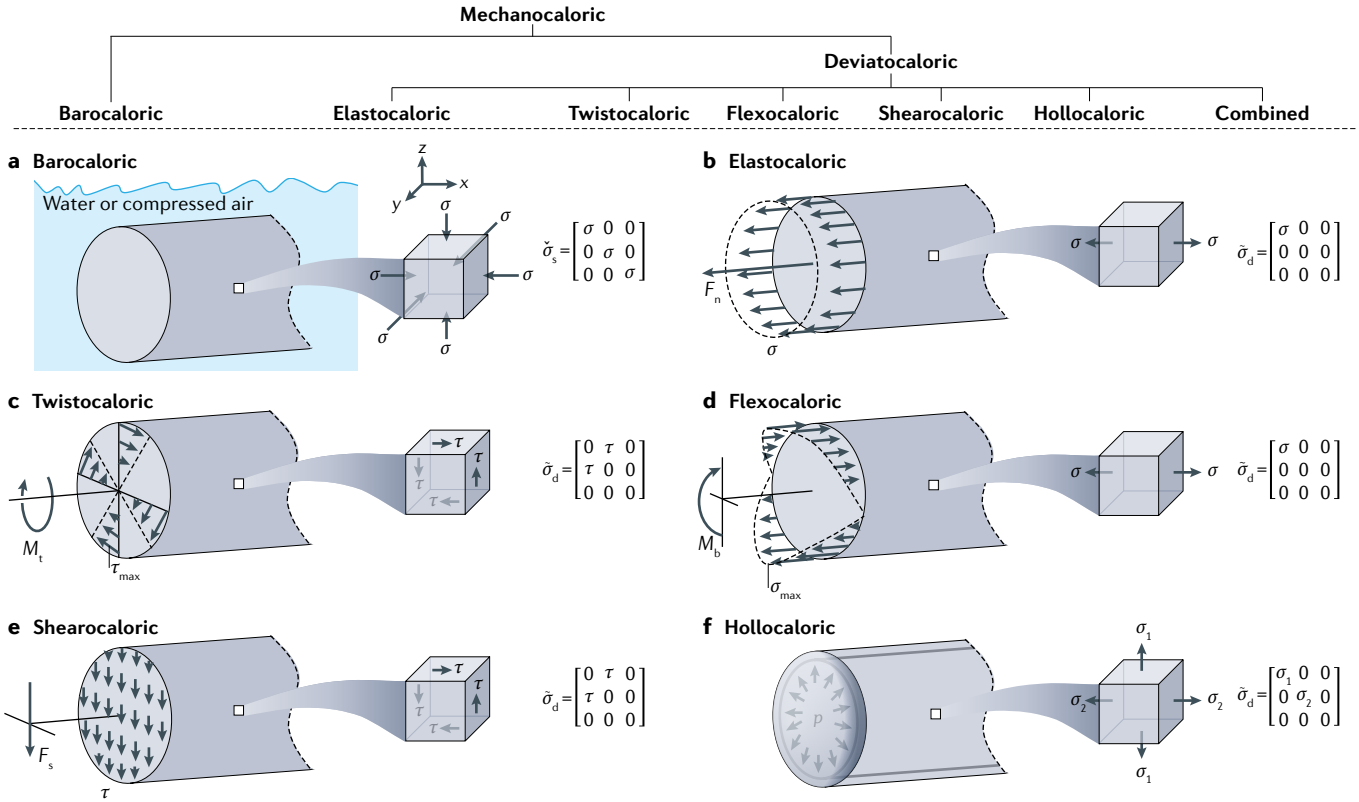


multicaloric cycles can suppress extrinsic hysteresis in multi-stimulus loops by leveraging the sensitivity of a ferroic transformation to a non-conjugate field. For instance, the onset and pathway of a magnetic transition can be tuned by the application of stress. In one example, a notable reduction in magnetic hysteresis was observed in $Ni_{45.2}Mn_{36.7}In_{13}Co_{5.1}$ at 308 K when it was magnetized at 7 T under zero pressure and the magnetic field was then removed under a pressure of 130 MPa (REF.[9]). Similarly, the reduction in magnetic hysteresis in $Fe_{50}Rh_{50}/BaTiO_3$ was achieved by first magnetizing the composite in a 5-T magnetic field with zero electric field at 385 K, before applying an electric field of 0.2 MV m$^{-1}$ to $BaTiO_3$ and subsequently removing first the magnetic field and then the electric field[99]. We note that, in both cases, the hysteresis is simply shifted to a different field variable and the overall dissipative energy losses are not diminished.

Box 2 | **Impact of hysteresis on functional fatigue**

The dissipated energy percentage ($\frac{\Delta}{\Phi}$) is the ratio of the dissipative energy losses manifested as the field loop hysteresis area ($\Delta$) (see the figure, blue regions) to the stored energy by input work ($\Phi$) (see the figure, grey striped regions), in first-order phase-transformation materials. $\frac{\Delta}{\Phi}$ measures how much of the stored energy is lost as dissipative energy, which correlates well with the functional fatigue behaviour of the material. Dissipative energy losses during the transformation process can decrease the fatigue lifetime of a material and various strategies[11,142,163,164,272,302–309] have been proposed to reduce the hysteresis and, thus, increase the durability (see the table and Supplementary Table 7). The stored energy from the work by the external fields during the forward transformation provides the potential energy for the reverse transformation and high stored energy increases the threshold for irreversibility and increases the endurance limit.

First identified in elastocaloric materials, there is a trend between minimizing the ratio, $\frac{\Delta}{\Phi}$, and extending the functional lifetime, $N_f$ (the number of sustained cycles). Four materials cases are illustrated in panel **b** of the figure in order of optimization level. The large or medium $\Phi$ and $\Delta$ and large $\frac{\Delta}{\Phi}$ of materials 1 and 2 are unfavourable for a long functional lifetime. By contrast, material 3 has medium $\Phi$, small $\Delta$ and small $\frac{\Delta}{\Phi}$, which are favourable for a long functional lifetime. The ideal case is material 4, which has small $\Phi$, minimal $\Delta$ and minimal $\frac{\Delta}{\Phi}$, and is the most likely to display a long functional lifetime. A low critical transformation field, $X_c$ (see the figure, dashed line in panel **a**), is favourable because it makes it easier to drive the transformation of the materials. From an energetics point of view, the same principle is expected to apply to other caloric processes involving magnetic, electric or combined fields.

**Approaches to reduce hysteresis in first-order-type caloric materials**

| Caloric process | Strategy | Mechanism | Refs |
|---|---|---|---|
| Elastocaloric | Tune composition | Increases interface compatibility through lattice matching | 141,157,269,270 |
| Magnetocaloric | Partial substitution of chemical elements | Weakens itinerant-electron metamagnetic transition | 142,152,310,311 |
| Electrocaloric | Unipolar cycling | Incomplete reversal minimizes the formation of polarization domains | 144,255,307–309,312 |
| Multicaloric | Introduce non-conjugate fields | Overlaps one original loop with another loop shifted under a non-conjugate field to form an intersected loop | 9,99,100 |

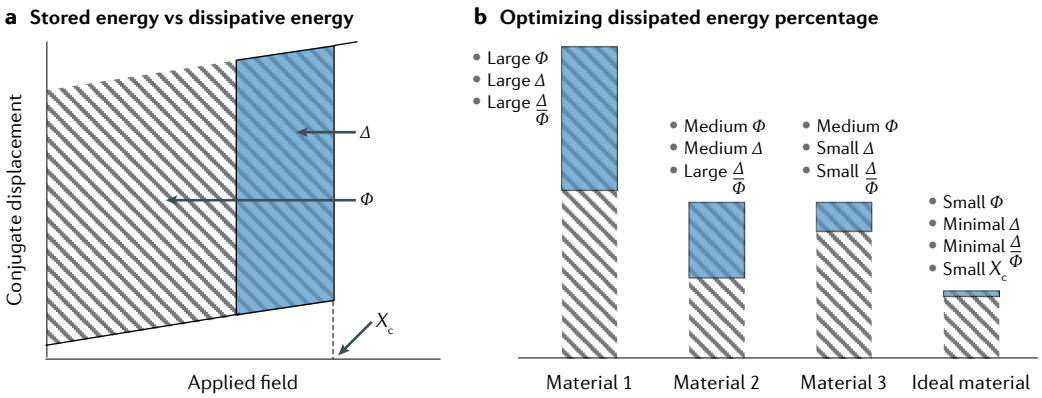


The energy dissipated as hysteresis in a back-and-forth transformation process is not the only mechanism that influences the functional fatigue life in phase-transforming materials. For elastocaloric alloys, it was proposed that the stored elastic energy that accumulates in the forward transformation provides the driving force for the reverse transformation, eliminating the need to lower the critical reverse transformation stress[163,164]. Furthermore, a high stored elastic energy increases the threshold for irreversible deformations and increases the transformation reversibility (a measure of transformation efficacy)[165] if the accommodation of the shape and volume changes between phases accompanies a strong slip resistance of the high-temperature phase[166], namely, a high yield strength. The endurance limit of a material subjected to stress has a monotonic correlation with the mechanical strength for materials ranging from metals and polymers (with a correlation coefficient of 0.33) to ceramics and glasses (with a correlation coefficient of 0.9)[167]. For electrocaloric and magnetocaloric materials, the equivalent upper limits for the endurance are dielectric strength and breakdown magnetostriction, respectively[3].

When the dissipated energy associated with the hysteresis is divided by the stored energy, one obtains a dimensionless quantity called 'dissipated energy percentage'[11], which provides a direct measure to monitor and predict the functional lifetime of first-order phase-transforming materials. A qualitative relation between the dissipated energy percentage ($\frac{\Delta}{\Phi}$) and functional lifetime can be expressed as:

$$N_f \propto \left(\frac{\Delta}{\Phi}\right)^{-1} \quad (1)$$

where $N_f$ is the number of sustained cycles (that is, the number of cycles until the onset of loss of functionality)[11], $\Delta$ is the hysteresis area enclosed by the field loop and $\Phi$ is the stored energy per unit volume per field cycle. The qualitative relation in Eq. 1 captures a trend in a series of elastocaloric materials (Supplementary Fig. 1), in which lowering $\frac{\Delta}{\Phi}$ extends the functional lifetime of the materials. When $\frac{\Delta}{\Phi}$ is below a threshold of ~10%, an $N_f$ of more than one million is observed[11].

The concept of dissipated energy and stored energy can be extended from elastocaloric materials to other caloric materials (BOX 2), including magnetocaloric and electrocaloric materials, the fatigue-related properties of which are receiving increasing attention[143,144,168–172]. For example, a magnetocaloric material $MnFe_{0.95}P_{0.595}B_{0.075}Si_{0.33}$ with a $\frac{\Delta}{\Phi}$ of 2.8% survived for >10,000 cycles with a $\Delta T_{ad}$ of 2.55 K (REFS[143,173]). Nanostructured polycrystalline $(La_{0.6}Ce_{0.4})_2Fe_{11}Si_2H_y$ with a $\frac{\Delta}{\Phi}$ of ~1% sustained $10^5$ cycles with a $\Delta T_{ad}$ of 2.2 K (REF.[174]), and porous polycrystalline $LaFe_{11.6}Si_{1.4}$ with a $\frac{\Delta}{\Phi}$ of 20.0% exhibited a $\Delta T_{ad}$ of 7.3 K over 800 cycles[172]. An electrocaloric $Pb(Mg_{1/3}Nb_{2/3})O_3$ relaxor with a $\frac{\Delta}{\Phi}$ of 23.0% was cycled 70,000 times with a $\Delta T_{ad}$ of 1.2 K, whereas single-crystal $BaTiO_3$ with a large $\frac{\Delta}{\Phi}$ of 83.1% started degrading after 10 cycles[175].

Several materials with a $\frac{\Delta}{\Phi}$ below 10% have demonstrated stability over $10^6$ cycles. Electrocaloric $Ba(Zr_{0.2}Ti_{0.8})O_3$ ceramics with a $\frac{\Delta}{\Phi}$ of 9.5% exhibited a $\Delta T_{ad}$ of 0.2 K under unipolar cycling at 20 kV cm$^{-1}$, with the polarity of the electric field reversed every $10^5$ cycles to maintain the $\frac{\Delta}{\Phi}$ to reach $10^6$ cycles[170]. Electrocaloric PMN–10PT bulk relaxor ceramics with a $\frac{\Delta}{\Phi}$ of 5.5%[15,169] exhibited a $\Delta T_{ad}$ of 1.3 K for $10^6$ cycles during unipolar cycling at 90 kV cm$^{-1}$. Magnetocaloric $La(Fe_{0.865}Co_{0.05}Si_{0.085})_{13}$ alloys with a $\frac{\Delta}{\Phi}$ of 7.0%[171,176] that were cycled with a magnetic field change of 0.6 T exhibited a $\Delta T_{ad}$ of 0.5 K for $10^6$ cycles when protected from exposure to air (by contrast, samples failed within 24 h in air or within 1 h in distilled water with 0.1 M $Na_2WO_4$, owing to corrosion). As a benchmark, if a material used in a cooling appliance is to survive for a typical commercial product lifetime of 10 years, it must sustain performance for at least 78 million cycles operating at 1 Hz, assuming it is used for 6 months per year and 12 h a day.

The relation in Eq. 1 should, in principle, apply to second-order phase-transforming materials, in which apparent minimal hysteresis translates to infinitely long functional lifetimes (although, in practice, all materials have finite operational lifetimes). Reducing $\frac{\Delta}{\Phi}$ can extend the number of cycles over which monocaloric materials are stable (Supplementary Fig. 1) and, in principle, is a viable strategy for increasing the durability of multicaloric materials to meet the performance requirements of commercial cooling devices. Ideally, not only should the field hysteresis of multicaloric materials be reduced by, for example, introducing non-conjugate fields (see the table within BOX 2) but the dissipative energy losses and $\frac{\Delta}{\Phi}$ should also be minimized (see panel **a** of the figure in BOX 2). It is preferable that a full transformation accompanying such a minimization can be achieved at a low critical transformation field (see panel **b** of the figure in BOX 2), which can enable easy driving of the phase transformation in the materials using less bulky equipment and, thus, facilitate the design of compact devices.

## Technological potential of multicalorics

In this section, we examine the technological advantages of multicaloric cooling, with an eye towards the development of prototype systems. In TABLE 1, we list some of the best experimentally observed values of relevant properties of monocaloric materials, which can serve as the baseline for multicaloric cooling techniques and systems. The potential benefits of multicaloric cooling over monocaloric cooling are the possibilities of enhancing numerous properties, as well as widening operational parameters, namely, increasing thermal properties ($\Delta T_{ad}$, $\Delta S$ and the refrigerant capacity), widening the operating temperature window (OTW), reducing the field hysteresis ($\Delta X$) and lowering the driving field.

Elastocaloric materials exhibit some of the largest values of $\Delta T_{ad}$, the widest OTW and the largest $N_f$, but require driving fields of several hundred megapascals (TABLE 1), which makes it difficult to fabricate small prototype devices. Elastocaloric effects have a major role in multicaloric operations, in which the application of multiple fields can achieve sizable caloric effects at a lower driving field. For example, using a quasi-direct method, the elastocaloric $\Delta T_{ad}$ of $Ni_{50}Mn_{35.5}In_{14.5}$ was shown to increase by 100%, from 1.25 K at a constant magnetic field of 0 T to 2.5 K at constant 4 T, upon varying the applied stress by 40 MPa. However, the magnetocaloric $\Delta T_{ad}$ decreased by 12.2%, from 4.9 K at constant 0 MPa to 4.3 K at constant 40 MPa, upon varying the magnetic field by 4 T (REF.[108]). The elastocaloric OTW in PMN–32PT single crystals increased by 62.5%, from 40 K to 65 K, upon application of an electric field of 1.5 MV m$^{-1}$ (REFS[177,178]). In Ni–Mn-based alloys[179,180], one can leverage the OTW of the elastocaloric effect in one temperature range and the OTW of the magnetocaloric effect in another range to maximize the overall OTW.

The coexistence of ferroic order parameters, however, is not always an advantage when trying to harness the entropy change from both degrees of freedom through multicaloric processes. The presence of an inverse-caloric effect (due to entropy changes in opposite directions[111,181–183]) in a material can lead to a decrease in the observed caloric effect. For example, for the all-*d*-Heusler alloy $Ni_{37.0}Co_{13.0}Mn_{34.5}Ti_{15.5}$, a $\Delta T_{ad}$ of 17.7 K was achieved with a pulsed magnetic field of 10 T in the absence of a stress field; however, with a constant uniaxial load of 80 MPa, $\Delta T_{ad}$ decreases to 9.0 K under the same magnetic field[184]. It is the negative sign of the cross-susceptibility between multiple degrees of freedom in such a multiferroic material that can be detrimental to the overall entropy change. Therefore, close inspection of the complex energy landscape governed by coupled order parameters is necessary when trying to use single-phase materials (quadrant II in FIG. 2a) for multicaloric cooling.

For caloric cooling technologies, the road between fundamental materials science and widespread commercialization has to be paved with innovations in device engineering and prototype development. Primarily based on linear or rotary drive principles, more than

Table 1 | **Best-reported properties of monocaloric cooling materials and systems near room temperature, and the potential for improvement with multicaloric**

| Monocaloric | | Multicaloric | |
|---|---|---|---|
| **Type** | **Best experimentally reported values** | **Reported examples[a]** | **Potential** |
| ***Materials: adiabatic temperature change (\|ΔTad\|) by direct experimental measurement*** | | | |
| mC | 17–58 K (elastocaloric)[34,72,74,226,227] | $Ni_{49.3}Mn_{34.8}In_{15.9}$: 2.4 K (magnetic field: 0 → 1 T; stress field (triaxial): 0 → 490 MPa) (category II)[109] | ↑ |
| | ~6.5–16.4 K (barocaloric)[78,228,229] | | |
| | 20.8 K (twistocaloric)[132] | | |
| | 8.1–15.4 K (flexocaloric)[134,135,137] | $Ni_{37.0}Co_{13.0}Mn_{34.5}Ti_{15.5}$: −9.0 K (magnetic field: 0 → 10 T; stress field (uniaxial): constant 80 MPa) (category II)[184] | |
| MC | 6.2–12.9 K (quasi-static fields)[230–232] | | |
| | 15.0 K at 7.5 T (REF.[233]); 60.5 K at 62 T (REF.[234]); 60.0 K at 55 T (REF.[235]); 20.0 K at 50 T (REF.[236]) (pulsed fields) | | |
| EC | 2.1–5.5 K (bulk)[10,237–243] | | |
| | 12 K at 170 MV m$^{-1}$ (REF.[244]) and 120 MV m$^{-1}$ (REFS[40,244]); 40 K at 125 MV m$^{-1}$ (REF.[245]); 20 K at 160 MV m$^{-1}$ (REF.[245]) (thin film) | | |
| ***Materials: isothermal entropy change (\|ΔS\|) normalized by mass*** | | | |
| mC | ~60–70.7 J kg$^{-1}$ K$^{-1}$ (elastocaloric)[246,247] | Fe–Rh/PMN–PT composite: 15.6 J kg$^{-1}$ K$^{-1}$ (magnetic field: 0 → 5 T; electric field: constant −0.6 MV m$^{-1}$) (category IV)[101] | ↑ |
| | 510 J kg$^{-1}$ K$^{-1}$ (barocaloric)[86] | | |
| MC | ~18–47.3 J kg$^{-1}$ K$^{-1}$ (REFS[31,48,51,248–253]) | | |
| EC | ~3.1–8.0 J kg$^{-1}$ K$^{-1}$ (bulk)[254–256] | | |
| | 130 J kg$^{-1}$ K$^{-1}$ (thin film)[257] | | |
| ***Materials: refrigerant capacity*** | | | |
| mC | ~2,300 J kg$^{-1}$ (elastocaloric)[258] | $Ni_{43}Mn_{40}Sn_{10}Cu_7$: 6.0 J kg$^{-1}$ (stress field (uniaxial): 0 → 5.24 MPa; magnetic field: constant 0.87 T) (category II)[111] | ↑ |
| | ~2,500–2,700 J kg$^{-1}$ (barocaloric)[85,229] | | |
| MC | ~300–1,346 J kg$^{-1}$ (REFS[142,259–261]) | | |
| EC | 130 J kg$^{-1}$ (bulk)[262] | | |
| | 662–2,000 J kg$^{-1}$ (thin film)[245,263] | | |
| ***Materials: operating temperature window*** | | | |
| mC | ~130 K (elastocaloric)[258] | $Fe_{49}Rh_{51}$: 50 K (magnetic field: 0 → 2 T; hydrostatic pressure: 500 → 0 MPa) (category II)[181] | ↑ |
| | ~60 K (barocaloric)[85] | | |
| MC | ~40–60 K (REFS[31,142,264–266]) | | |
| EC | ~30–60 K (REFS[256,267,268]) | | |
| ***Materials: hysteresis (ΔX) by first-order phase transition*** | | | |
| mC | ~0–2 K (elastocaloric, thermal)[157,269] | Fe–Rh/$BaTiO_3$ composite: 96% reduction in hysteretic losses in dual-stimulus field loops (magnetic field: 0 → 5 T; electric field: constant 0.2 MV m$^{-1}$) (category IV)[99] | ↓ |
| | ~0–900 × 10$^3$ J m$^{-3}$ (elastocaloric, field loop)[11,73,270–272] | | |
| MC | ~1 K (thermal)[31] | | |
| | ~0 J m$^{-3}$ (field loop)[102,142] | | |
| EC | ~2 K (thermal)[273] | | |
| | ~0–70 × 10$^3$ J m$^{-3}$ (field loop)[10,144,274] | | |
| ***Materials: fatigue life in number of sustained cycles (Nf)*** | | | |
| mC | 10$^6$–10$^9$ cycles at $\Delta T_{ad}$ > 4 K (elastocaloric)[11,270,275–278] | NA | ↑ |
| MC | 9 × 10$^4$ cycles at $\Delta T_{ad}$ = 1.9 K (REF.[279]); 10$^3$ cycles at $\Delta T_{ad}$ = 0.5 K (REF.[171]) | | |
| EC | 10$^6$ cycles at $\Delta T_{ad} \approx$ 1.5 K (REF.[144]), $\Delta T_{ad}$ = 1.3 K (REF.[169]) and $\Delta T_{ad}$ = 0.3 K (REF.[170]) | | |
| ***Systems: driving field*** | | | |
| mC | ~300–600 MPa (elastocaloric)[14,280–282] | Proposed prototype: a sequence of magnetic field 0 → 2 T and stress field (uniaxial) 0 → 80 MPa on $Ni_{49.3}Mn_{34.8}In_{15.9}$ for a cooling effect similar to that with a magnetic field of 0 → 4 T alone (category II)[121] | ↓ |
| MC | ~1–1.5 T (REFS[13,189,283–286]) | | |
| EC | ~10–100 MV m$^{-1}$ (REFS[15,62–64,197,287–289]) | | |

Table 1 (cont.) | **Best-reported properties of monocaloric cooling materials and systems near room temperature, and the potential for improvement with multicalorics**

| Monocaloric | | Multicaloric | |
|---|---|---|---|
| **Type** | **Best experimentally reported values** | **Reported examples[a]** | **Potential** |
| ***Systems: cooling power for a given mass of refrigerant*** | | | |
| mC | 65 W with $1.05 \times 10^{-1}$ kg (REF.[77]); 7.9 W with $1.26 \times 10^{-3}$ kg (REF.[290]) (elastocaloric) | NA | ↑ |
| MC | 3,042 W with 1.52 kg (REF.[13]) | | |
| EC | 0.64 W with $2.3 \times 10^{-4}$ kg (REF.[64]); 0.26 W with $2.2 \times 10^{-2}$ kg (REF.[62]) | | |
| ***Systems: regenerator temperature span*** | | | |
| mC | 15.3–19.9 K (elastocaloric)[14,291,292] | NA | ↑ |
| MC | 33–45 K (REFS[293–295]) | | |
| EC | 6.6–13.0 K (REFS[62,65,197]) | | |
| ***Systems: operating frequency*** | | | |
| mC | 0.125–4 Hz (elastocaloric)[14,77,280,291,296,297] | NA | – |
| MC | 0.5–4 Hz (REFS[13,187,189,283,298–300]); 20 Hz (REF.[223]) | | |
| EC | 0.15–1.25 Hz (REFS[15,63,197]) | | |

For the materials, the metrics are for those that exhibit first-order phase transitions and have been experimentally measured using a direct method. The systems' performance parameters are for various prototype devices. Within a specific caloric cooling device, the system performance depends on the operating parameters during the optimization. Owing to the complex influence of the operating parameters, we qualitatively present the system coefficient of performance ($COP_{system}$) in FIG. 3. The potential for multicalorics to increase or decrease the best-reported property values are denoted by an upwards arrow or a downwards arrow, respectively, and a dash indicates that there are no clear pathways to increase or decrease a property at present. Unless otherwise specified, the largest values of cooling power are at zero temperature span and the largest temperature spans are at zero cooling power. EC, electrocaloric; mC, mechanocaloric; MC, magnetocaloric; NA, no available data; PMN–PT, $Pb(Mg_{1/3}Nb_{2/3})O_3$–$PbTiO_3$.
[a]Additional examples of multicalorics are given in Supplementary Table 1.

80 prototypes of magnetocaloric systems have been constructed to date, with the cooling power ranging from a few watts to thousands of watts[13,16,42]. In particular, magnetocaloric wine coolers were showcased jointly by Haier, Astronautics and BASF at the International Consumer Electronics Show in Las Vegas in 2015 (REF.[185]), a comprehensive assessment of a 31-bottle wine cooler cabinet was reported in 2020 (REF.[186]) and a magnetocaloric proof-of-concept unit was piloted for an industrial partner in 2021 (REF.[187]). There has also been a report of the operation of a 65-W elastocaloric prototype[77]. To the best of our knowledge, there is yet to be a demonstration of a prototype system based on multicaloric operation.

For a given set of operation temperatures, $T_c$ and $T_h$, which are the temperatures of the heat source and the heat sink, respectively, one can compare the efficiency of an instrument to convert input work into cooling power, measured by the COP for a refrigeration or heat-pump system. The ratio of the COP to the Carnot COP ($COP_{Carnot}$), which is the theoretical upper limit defined by the second law of thermodynamics for delivering cooling at $T_c$ while rejecting heat at $T_h$, represents the ultimate measure of thermodynamic performance. State-of-the-art commercial, vapour-compression systems, such as factory-made air conditioners, typically exhibit a system COP ($COP_{system}$) of 2–4 at $T_h = 308$ K and $T_c = 300$ K (consistent with the air-to-air temperatures in the typical standards used to assess such systems: AHRI Standard 210/240 and United States Code of Federal Regulations (CFR) 430.32). There have been very few reports of the $COP_{system}$ of caloric cooling systems[53,188,189], which reflects the challenges associated with constructing systems and performing accurate measurements of the $COP_{system}$. These challenges are augmented if multiple fields need to be applied, and include the difficulty in controlling the sequence in which multiple driving fields are applied and coordinating with the flow of the heat-exchange fluid. The concept of a rotatory multicaloric system was recently proposed and featured work recovery and field coordination, enabling versatile operations for a large temperature span[190].

Nevertheless, because of the latest developments in caloric materials and devices, as well as the advent of multicaloric cooling schemes, there are reasons to be optimistic that multicaloric cooling technologies can be realized. Here, we present a systematic approach (FIG. 3) to analyse and estimate the achievable $COP_{system}$ of multicaloric cooling systems based on a formalism that we previously developed for monocaloric cooling systems[191]. All COP values have been calculated for a given set of $T_c$ and $T_h$ and compared against $COP_{Carnot}$. $COP_{Carnot}$ is 37.5 for $T_h = 308$ K and $T_c = 300$ K, which are the temperatures used here in consideration of applications near room temperature. The first COP to consider is the materials COP ($COP_{mat}$), which is a measure of the intrinsic efficiency of the heat-pumping process at the materials level and represents the potential of the materials to achieve efficient cooling when implemented in a device. Against $COP_{mat}$, we then consider various extrinsic loss mechanisms that arise owing to necessary components that are 'added' to the material. These losses are the field-driving loss, heat-transfer loss, cyclic loss and parasitic power loss, which all depreciate the starting $COP_{mat}$. The Stirling cycle is among the best-known thermodynamic cycles for caloric cooling and possesses

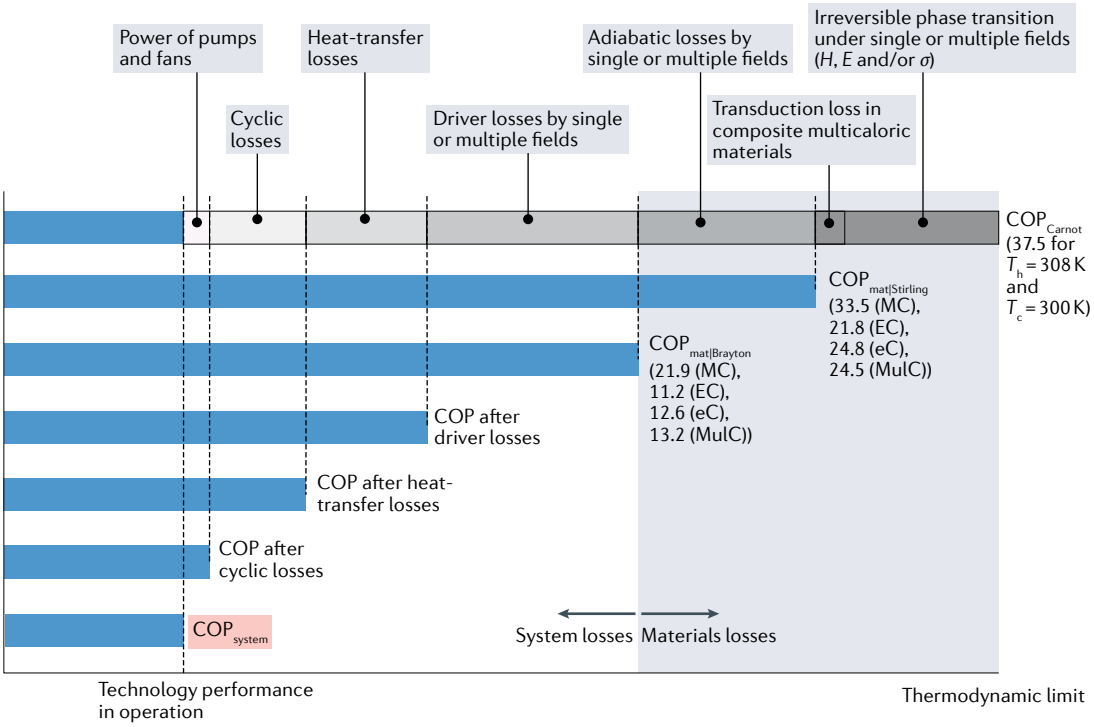


Fig. 3 | **Loss factors in monocaloric and multicaloric cooling systems.** Various losses occur in functioning caloric technologies. The coefficient of performance (COP) of the ideal Carnot cycle ($COP_{Carnot}$) represents the thermodynamic limit. The materials COP for the Stirling cycle ($COP_{mat|Stirling}$) considers the irreversibility of field-induced phase transitions and represents the efficiency potential of materials. The materials COP for the Brayton cycle ($COP_{mat|Brayton}$) takes into account the irreversibility of adiabatically applying and removing the stimulating fields to a material. The system losses comprise four components: losses in the drive mechanisms that generate stimuli fields; heat-transfer losses between the caloric material and a transfer medium, which limit the extraction of full caloric latent heat; losses during cyclic operations, owing to dead thermal mass decreasing the transport of caloric latent heat; and parasitic power dissipation attributable to auxiliary parts, such as pumps, fans, valves and control boards. The final technology performance is $COP_{system}$ (highlighted in red). Compared with a single-phase caloric system (monocaloric or multicaloric), a composite caloric system might have an additional loss due to transduction between the composite components. The highest reported and estimated $COP_{mat}$ of elastocaloric (eC), magnetocaloric (MC), electrocaloric (EC) and multicaloric (MulC) materials are listed (see Supplementary Notes 2,3 and Supplementary Table 6 for further details). A heat-source temperature ($T_c$) of 300 K and a heat-sink temperature ($T_h$) of 308 K were chosen based on the AHRI Standard 210/240 performance rating for unitary air conditioning and air-source heat-pump equipment, in which a typical vapour-compression-based air conditioner has a $COP_{system}$ in the range 2–4.

a higher efficiency than other cycles, because the isothermal field-variation processes and the iso-displacement regenerative processes have low irreversible losses and, thus, minimize the cycle area in the temperature–entropy diagram[42]. Thus, the Stirling cycle can be used to screen caloric materials in which irreversible phase transitions are the loss factor relative to the Carnot cycle (FIG. 3). The $COP_{mat}$ for a single-phase monocaloric material in a Stirling cycle subjected to a single external field, $X$ (I.1–I.3 in FIG. 2d), can be expressed as

$$COP_{mat|Stirling,X} = \frac{T_c\Delta s_X - T_c s_{gen,X}}{(T_h - T_c)\Delta s_X + (T_h + T_c)s_{gen,X}} \quad (2)$$

where $\Delta s_X = \Delta s(T_0, 0 \rightarrow X)$ is the field-induced specific entropy change,

$$s_{gen,X} = \frac{\oint_0^X dw|_{T=T_0}}{2T_0} \quad (3)$$

is the specific entropy generated owing to the irreversibility of the phase transition and $w$ is the specific work during an isothermal test at the temperature $T_0$. In this manner, $COP_{mat}$ can be determined using basic materials properties, and, experimentally, values as high as ~80% of $COP_{Carnot}$ have been observed[34]. Similarly, for a single-phase multicaloric material, $COP_{mat}$ in a Stirling cycle subjected to two fields, $X_1$ and $X_2$ (II.1–II.4 in FIG. 2d), can be expressed as

$$COP_{mat|Stirling,X_1+X_2} = \frac{T_c\Delta s_{X_1+X_2} - T_c s_{gen,X_1+X_2}}{(T_h - T_c)\Delta s_{X_1+X_2} + (T_h + T_c)s_{gen,X_1+X_2}} \quad (4)$$

where $\Delta s_{X_1+X_2} = \Delta s(T_0, (0,0) \rightarrow (X_1, X_2))$,

$$s_{gen,X_1+X_2} = \frac{\oint_0^{X_1} dw_1|_{T=T_0} + \oint_0^{X_2} dw_2|_{T=T_0}}{2T_0} \quad (5)$$

and $w_1$ and $w_2$ are the specific work by fields $X_1$ and $X_2$ during an isothermal test at temperature $T_0$, respectively. In practical operation in devices, instead of the isothermal operations in Eqs 2 and 4, caloric heat-pumping processes are often driven by the adiabatic application and removal of fields for ease of operation, and the Brayton cycle is most commonly applied. In addition to the losses in the materials themselves, as considered in the Stirling cycle, the Brayton cycle involves cycle-related irreversibility as an additional loss arising from the adiabatic application and removal of fields (FIG. 3). One can similarly derive $COP_{mat}$ in Brayton cycles (see Supplementary Notes 2,3 and Supplementary Tables 3–6 for derivations and data for both cycles). In FIG. 3, we list some of the largest reported values of $COP_{mat}$ for Stirling and Brayton cycles.

Because of the diversity of ways in which caloric cooling can be realized in devices and heat exchange implemented, as well as the variety of losses in systems, it becomes difficult to calculate a COP value after the four loss mechanisms, which successively decrease $COP_{mat}$. The key message of FIG. 3, however, is that, given that the starting $COP_{mat}$ is as high as 20–30 for caloric materials, if the aim is to have a final $COP_{system}$ of >4, the difference represents challenges — and opportunities — for the development of highly efficient systems to rival vapour-compression systems.

## Future perspectives

The drive to increase efficiency and minimize the environmental impact of refrigerants continues to motivate innovations in cooling technologies. The advances in multicaloric materials and devices could enable solid-state cooling technology to reach the technological threshold for commercialization. Just as developments in magnetocaloric materials in the late 1990s fuelled their scientific pursuit and industrial interest[48,192,193], we believe that multicaloric cooling is today poised to lead the next decades of innovations in caloric cooling.

We envisage that advances in multicaloric cooling will be made possible by improvements in materials properties, such as a reduction in hysteresis, as well as the optimization of application schemes for multiple external fields. As the concept of active regeneration first developed for magnetocaloric cooling[47,194,195] has now been adopted by the other caloric cooling techniques[14,62,196,197], we expect active multicaloric regeneration and even more advanced cross-disciplinary approaches to give rise to new cooling-system prototypes. From additive manufacturing to the intelligent design of heat exchangers, advanced materials processing techniques are expected to be the linchpin for the production of active solid refrigerants and other components for system assembly.

Given the existing and impending global regulations of hydrofluorocarbons, and the limited options for suitable replacements[198,199], it is anticipated that caloric and multicaloric cooling systems will become more popular and viable, with the potential to penetrate the commercial market. In particular, when the footprint of caloric cooling devices becomes scalable, they are expected to be competitive in small-sized applications, in which the volume-specific latent heat from phase transitions in caloric cooling is extremely favourable compared with that of vapour compression. For instance, the latent heat of a $Ni_{49.8}Ti_{30.2}Hf_{20}$ alloy[75,200] is hundreds of J cm$^{-3}$, which is orders of magnitude higher than that of vapour compression (single-digit J cm$^{-3}$ with R-134a and ~10 J cm$^{-3}$ with R-32, the typical commercial refrigerants, normalized by the specific volume of the vapour phase[201]). A high value or, more technically, a high volumetric refrigeration capacity[198], indicates the potential for a compact system.

Beyond mainstream heating, ventilation and air conditioning applications, multicaloric cooling may find transformative applications in emerging high-tech fields. One example is the implementation of the magneto-elastocaloric effect (III.1 in FIG. 2d) for remote focal brain cooling to treat epileptic seizures[103,202], which requires a small spot in the neocortex to be cooled by ~10 K for a short period of time[203–205], and is aligned with the objectives of brain–machine interfaces advanced by Neuralink[206]. The device is compact (~11.5 × 2.8 × 2.8 cm$^3$), which is made possible by the ultralow magnitude of the magnetic field (~0.16 T). It is the compact footprint of such a multicaloric device configuration that enables new cooling applications. Another possible application of the magneto-elastocaloric effect is hydrogen liquefaction: active regenerative liquefiers based on a pure magnetocaloric effect currently use high magnetic fields (1.8–6 T)[207–212] but, using a composite device, cost-effective and efficient liquefaction might be realized at lower fields. The application of a mechanical field can reduce the need for a high magnetic field by partnering with a low magnetic field to achieve a similar caloric effect[121].

Although there have been many recent advances in caloric technology, two areas have shown substantial progress, namely, additive manufacturing and regenerative processes.

***Additive manufacturing of caloric materials and devices.*** Additive manufacturing uses a digital design to guide an energy source to consolidate feedstock materials layer by layer to build a 3D object[213–215]. This approach can overcome the challenges associated with the fabrication of complex regenerator architectures with a large surface-to-volume ratio, which is desirable for efficient heat transfer. Moreover, it is possible to build the intricate and complex geometrical structures needed for the application of multiple fields in composite multicaloric processes (IV.1–IV.4 in FIG. 2d).

Additive manufacturing has already been implemented to advance caloric technology. For example, selective laser melting was used to print wavy-channel blocks and fin-shaped rods of magnetocaloric $La(Fe,Co,Si)_{13}$ (REF.[171]), as well as double-corrugated flow structures and straight flow channels of magnetocaloric $La_{0.84}Ce_{0.16}Fe_{11.5}Mn_{1.5}Si_{1.3}H_x$ (REF.[216]). Directed-energy deposition offers the advantage of stoichiometric control of the feedstock and was used to engineer the eutectic nanocomposite microstructure of Ni–Ti-based elastocaloric materials to achieve high materials efficiency and an extended fatigue life[11]. This technique was also used to make magnetocaloric $AlFe_2B_2$ compounds in rod and honeycomb structures[217]. In addition to enabling the

fabrication of complex geometries, additive manufacturing may also offer solutions to some materials issues, such as brittleness in magnetocaloric alloys, by enabling precise manipulation of microstructure using a rapid cooling rate in a highly localized region.

Innovation could be advanced by integrating additive manufacturing with artificial intelligence[218–220] to establish an autonomous fabrication framework. In this framework, the objective of topological optimization in multicaloric regenerators will be addressed by coordinating machine learning algorithms and robotic hardware with the capacity to in situ monitor and qualify the performance with an iteratively developed database. Such a system can autonomously provide feedback using physics-based and data-based models in a closed-loop manner.

***Regenerative multicaloric cooling processes.*** Active regeneration bridges the limited materials $\Delta T_{ad}$ and the required temperature span of practical cooling devices[47], preferably ≥30 K (fluid-to-fluid temperature across the caloric regenerator), by periodically storing and transferring heat between a heat-transfer fluid and a regenerator made of caloric materials. Active regeneration establishes a lengthwise temperature profile by coupling the internal thermodynamic cycles of caloric materials arranged in series[42] and currently offers the best solution to increasing the temperature span in cooling systems. Advanced multicalorics with $\Delta T_{ad} \geq 30$ K in a single material (such as Ni–Mn–Ti alloys) (TABLE 1) have untold cooling capabilities and the potential to revolutionize solid-state cooling through their implementation in active regenerators. However, such a large starting $\Delta T_{ad}$ would require new mechanisms of pumping heat-transfer fluids. In active caloric regenerators, the mechanism of pumping heat-transfer fluids for convective heat transfer limits the operation frequency to several hertz owing to two main factors[41,221]: first, the limited work input from the pump constrains the velocity of the oscillation and the viscous fluid, and, second, convective heat transfer between the heat-transfer fluid and the caloric material is typically slow. Because the power output of a regenerator is proportional to the operating frequency, without advances in heat-transfer processes, the ultimate power output would be compromised[42,186], and the capabilities of the large $\Delta T_{ad}$ in materials cannot be fully harnessed.

One line of development of heat transfer in caloric devices is the introduction of thermal control elements, such as a thermal switch[221,222]. Control of the direction and, possibly, the intensity of heat flux in a short interval, approximately a millisecond, could notably increase the operating frequency and simultaneously maintain the efficiency achieved in active regeneration. The activation of a thermal switch by an external magnetic, electric or mechanical field, or their combination, could, in principle, be designed to occur in concert with the triggering of multicaloric effects to realize an anisotropic heat flow in single-stage, cascading or active regenerative schemes.

Another line of development is latent heat transfer by condensation and evaporation, which could make the transfer rate between heat exchangers and caloric materials an order of magnitude faster than that of conduction or convection[223,224] and, thus, enable a high operating frequency comparable with that of vapour compression. Magnetocaloric prototypes have demonstrated a tenfold increase in cycle frequency and specific cooling power by evaporating and condensing degassed methanol[223,225]. Such an approach indicates that advanced latent-heat-transfer processes might also be available for various multicaloric cooling techniques.

***Outlook.*** In less than 10 years after its inception, multicaloric cooling has become a promising research direction in solid-state cooling, with the potential for high energy-conversion efficiencies in addition to providing greener alternatives to existing technologies. Multicaloric cooling derives its functionalities from the rich physics of multiferroic materials, and its diverse range of embodiments represent possibilities for much-needed compact and environmentally friendly refrigeration technologies, as well as the development of new thermal device applications beyond conventional cooling technologies. Advances in the manufacturing of inexpensive materials with tailored properties and innovations in system designs for compact, high-performance cooling systems are expected to lower costs.

Published online 29 March 2022


1. Dupont, J. L., Domanski, P., Lebrun, P. & Ziegler, F. The role of refrigeration in the global economy (2019), 38th note on refrigeration technologies (International Institute of Refrigeration, 2019).
2. Fahler, S. et al. Caloric effects in ferroic materials: new concepts for cooling. *Adv. Eng. Mater.* **14**, 10–19 (2012).
3. Moya, X., Kar-Narayan, S. & Mathur, N. D. Caloric materials near ferroic phase transitions. *Nat. Mater.* **13**, 439–450 (2014).
4. Takeuchi, I. & Sandeman, K. Solid-state cooling with caloric materials. *Phys. Today* **68**, 48–54 (2015).
5. Cazorla, C. Novel mechanocaloric materials for solid-state cooling applications. *Appl. Phys. Rev.* **6**, 041316 (2019).
6. Moya, X. & Mathur, N. D. Caloric materials for cooling and heating. *Science* **370**, 797–803 (2020).
7. Goetzler, W., Zogg, R., Young, J. & Johnson, C. Energy savings potential and RD&D opportunities for non-vapor-compression HVAC technologies (Navigant Consulting, 2014).
8. Goetzler, W. et al. Energy savings potential and RD&D opportunities for commercial building HVAC systems (Navigant Consulting, 2017).
9. Liu, J., Gottschall, T., Skokov, K. P., Moore, J. D. & Gutfleisch, O. Giant magnetocaloric effect driven by structural transitions. *Nat. Mater.* **11**, 620–626 (2012).
10. Nair, B. et al. Large electrocaloric effects in oxide multilayer capacitors over a wide temperature range. *Nature* **575**, 468–472 (2019).
11. Hou, H. et al. Fatigue-resistant high-performance elastocaloric materials made by additive manufacturing. *Science* **366**, 1116–1121 (2019).
12. Sandeman, K. G. Research update: the mechanocaloric potential of spin crossover compounds. *APL Mater.* **4**, 111102 (2016).
13. Jacobs, S. et al. The performance of a large-scale rotary magnetic refrigerator. *Int. J. Refrig.* **37**, 84–91 (2014).
**Reports a magnetic refrigerator with a high cooling power on the order of kilowatts at both 0 K and over temperature spans of >10 K.**
14. Tušek, J. et al. A regenerative elastocaloric heat pump. *Nat. Energy* **1**, 16134 (2016).
**First demonstration of the applicability of active regeneration in elastocaloric prototyping.**
15. Plaznik, U. et al. Bulk relaxor ferroelectric ceramics as a working body for an electrocaloric cooling device. *Appl. Phys. Lett.* **106**, 043903 (2015).
16. Greco, A., Aprea, C., Maiorino, A. & Masselli, C. A review of the state of the art of solid-state caloric cooling processes at room-temperature before 2019. *Int. J. Refrig.* **106**, 66–88 (2019).
17. Mañosa, L. et al. Giant solid-state barocaloric effect in the Ni–Mn–In magnetic shape-memory alloy. *Nat. Mater.* **9**, 478–481 (2010).
18. Vopson, M. M. The multicaloric effect in multiferroic materials. *Solid State Commun.* **152**, 2067–2070 (2012).
19. Mañosa, L., Planes, A. & Acet, M. Advanced materials for solid-state refrigeration. *J. Mater. Chem. A* **1**, 4925–4936 (2013).
20. Stern-Taulats, E. et al. Multicaloric materials and effects. *MRS Bull.* **43**, 295–299 (2018).
21. Moya, X., Phan, M.-H., Srikanth, H. & Albertini, F. Multicalorics. *J. Appl. Phys.* **128**, 240401 (2020).
22. Lisenkov, S., Mani, B. K., Chang, C. M., Almand, J. & Ponomareva, I. Multicaloric effect in ferroelectric $PbTiO_3$ from first principles. *Phys. Rev. B* **87**, 224101 (2013).

23. Vopson, M. M. Theory of giant-caloric effects in multiferroic materials. *J. Phys. D* **46**, 345304 (2013).
24. Edström, A. & Ederer, C. Prediction of a giant magnetoelectric cross-caloric effect around a tetracritical point in multiferroic $SrMnO_3$. *Phys. Rev. Lett.* **124**, 167201 (2020).
25. Hao, J.-Z. et al. Multicaloric and coupled-caloric effects. *Chin. Phys. B* **29**, 047504 (2020).
26. Annaorazov, M. P., Nikitin, S. A., Tyurin, A. L., Asatryan, K. A. & Dovletov, A. K. Anomalously high entropy change in FeRh alloy. *J. Appl. Phys.* **79**, 1689–1695 (1996).
27. Eerenstein, W., Mathur, N. D. & Scott, J. F. Multiferroic and magnetoelectric materials. *Nature* **442**, 759–765 (2006).
28. Fiebig, M., Lottermoser, T., Meier, D. & Trassin, M. The evolution of multiferroics. *Nat. Rev. Mater.* **1**, 16046 (2016).
29. Ramesh, R. & Schlom, D. G. Creating emergent phenomena in oxide superlattices. *Nat. Rev. Mater.* **4**, 257–268 (2019).
30. Spaldin, N. A. & Ramesh, R. Advances in magnetoelectric multiferroics. *Nat. Mater.* **18**, 203–212 (2019).
31. Tegus, O., Bruck, E., Buschow, K. H. J. & de Boer, F. R. Transition-metal-based magnetic refrigerants for room-temperature applications. *Nature* **415**, 150–152 (2002).
32. Neese, B. et al. Large electrocaloric effect in ferroelectric polymers near room temperature. *Science* **321**, 821–823 (2008).
33. Bonnot, E., Romero, R., Mañosa, L., Vives, E. & Planes, A. Elastocaloric effect associated with the martensitic transition in shape-memory alloys. *Phys. Rev. Lett.* **100**, 125901 (2008).
34. Cui, J. et al. Demonstration of high efficiency elastocaloric cooling with large ΔT using NiTi wires. *Appl. Phys. Lett.* **101**, 073904 (2012).
35. Scott, J. F. Electrocaloric materials. *Annu. Rev. Mater. Res.* **41**, 229–240 (2011).
36. Franco, V. et al. Magnetocaloric effect: from materials research to refrigeration devices. *Prog. Mater. Sci.* **93**, 112–232 (2018).
37. Mañosa, L. & Planes, A. Materials with giant mechanocaloric effects: cooling by strength. *Adv. Mater.* **29**, 1603607 (2016).
**Analyses the thermodynamics of mechanocaloric effects and summarizes advances in the major families of barocaloric and elastocaloric materials**.
38. Qian, S. et al. A review of elastocaloric cooling: materials, cycles and system integrations. *Int. J. Refrig.* **64**, 1–19 (2016).
39. Shi, J. et al. Electrocaloric cooling materials and devices for zero-global-warming-potential, high-efficiency refrigeration. *Joule* **3**, 1200–1225 (2019).
40. Bruck, E., Yibole, H. & Zhang, L. A universal metric for ferroic energy materials. *Phil. Trans. R. Soc. A* **374**, 20150303 (2016).
41. Kitanovski, A. Energy applications of magnetocaloric materials. *Adv. Energy Mater.* **10**, 1903741 (2020).
42. Kitanovski, A. et al. *Magnetocaloric Energy Conversion* (Springer, 2015).
43. Weiss, P. & Piccard, A. Le phênomène magnêtocalorique. *J. Phys. Theor. Appl.* **7**, 103–109 (1917).
44. Debye, P. Einige Bemerkungen zur Magnetisierung bei tiefer Temperatur. *Ann. Phys.* **386**, 1154–1160 (1926).
45. Giauque, W. F. A thermodynamic treatment of certain magnetic effects. A proposed method of producing temperatures considerably below 1 ° absolute. *J. Am. Chem. Soc.* **49**, 1864–1870 (1927).
46. Giauque, W. F. & MacDougall, D. P. Attainment of temperatures below 1 ° absolute by demagnetization of $Gd_2(SO_4)_3 \cdot 8H_2O$. *Phys. Rev.* **43**, 768–768 (1933).
47. Brown, G. V. Magnetic heat pumping near room temperature. *J. Appl. Phys.* **47**, 3673–3680 (1976).
48. Pecharsky, V. K. & Gschneidner, K. A. Giant magnetocaloric effect in $Gd_5(Si_2Ge_2)$. *Phys. Rev. Lett.* **78**, 4494–4497 (1997).
49. Hu, F. X. et al. Influence of negative lattice expansion and metamagnetic transition on magnetic entropy change in the compound $LaFe_{11.4}Si_{1.6}$. *Appl. Phys. Lett.* **78**, 3675–3677 (2001).
50. Shen, B. G., Sun, J. R., Hu, F. X., Zhang, H. W. & Cheng, Z. H. Recent progress in exploring magnetocaloric materials. *Adv. Mater.* **21**, 4545–4564 (2009).
51. Krenke, T. et al. Inverse magnetocaloric effect in ferromagnetic Ni–Mn–Sn alloys. *Nat. Mater.* **4**, 450–454 (2005).
52. Masche, M., Liang, J., Dall'Olio, S., Engelbrecht, K. & Bahl, C. R. H. Performance analysis of a high-efficiency multi-bed active magnetic regenerator device. *Appl. Therm. Eng.* **199**, 117569 (2021).
53. Eriksen, D. et al. Design and experimental tests of a rotary active magnetic regenerator prototype. *Int. J. Refrig.* **58**, 14–21 (2015).
54. Dall'Olio, S. et al. Novel design of a high efficiency multi-bed active magnetic regenerator heat pump. *Int. J. Refrig.* **132**, 243–254 (2021).
55. Kobeko, P. & Kurtschatov, J. Dielectric properties of the Seignette salt crystals. *Z. Phys.* **66**, 192–205 (1930).
56. Wiseman, G. G. & Kuebler, J. K. Electrocaloric effect in ferroelectric Rochelle salt. *Phys. Rev.* **131**, 2023–2027 (1963).
57. Kikuchi, A. & Sawaguchi, E. Electrocaloric effect in $SrTiO_3$. *J. Phys. Soc. Jpn.* **19**, 1497–1498 (1964).
58. Hegenbarth, E. Studies of the electrocaloric effect of ferroelectric ceramics at low temperatures. *Cryogenics* **1**, 242–243 (1961).
59. Lombardo, G. & Pohl, R. O. Electrocaloric effect and a new type of impurity mode. *Phys. Rev. Lett.* **15**, 291–293 (1965).
60. Shepherd, I. & Feher, G. Cooling by adiabatic depolarization of $OH^-$ molecules in KCl. *Phys. Rev. Lett.* **15**, 194–198 (1965).
61. Mischenko, A. S., Zhang, Q., Scott, J. F., Whatmore, R. W. & Mathur, N. D. Giant electrocaloric effect in thin-film $PbZr_{0.95}Ti_{0.05}O_3$. *Science* **311**, 1270–1271 (2006).
62. Torelló, A. et al. Giant temperature span in electrocaloric regenerator. *Science* **370**, 125–129 (2020).
**Reports an electrocaloric device that uses active regeneration to achieve a temperature span of >10K**.
63. Wang, Y. et al. A high-performance solid-state electrocaloric cooling system. *Science* **370**, 129–133 (2020).
64. Ma, R. et al. Highly efficient electrocaloric cooling with electrostatic actuation. *Science* **357**, 1130–1134 (2017).
65. Meng, Y. et al. A cascade electrocaloric cooling device for large temperature lift. *Nat. Energy* **5**, 996–1002 (2020).
66. Gough, J. A description of a property of caoutchouc, or Indian rubber; with some reflections on the cause of the elasticity of this substance. *Mem. Lit. Philos. Soc. Manch.* **1**, 288–295 (1805).
67. Joule, J. P. On some thermo-dynamic properties of solids. *Philos. Trans.* **149**, 91–131 (1859).
68. Kobayashi, A. Elastocaloric effect in many-valley semiconductors. *J. Phys. Soc. Jpn* **17**, 1518–1518 (1962).
69. Bechtold, C., Chluba, C., De Miranda, R. L. & Quandt, E. High cyclic stability of the elastocaloric effect in sputtered TiNiCu shape memory films. *Appl. Phys. Lett.* **101**, 091903 (2012).
70. Quarini, J. & Prince, A. Solid state refrigeration: cooling and refrigeration using crystalline phase changes in metal alloys. *Proc. Inst. Mech. Eng. C J. Mech. Eng. Sci.* **218**, 1175–1179 (2004).
71. Rodriguez, C. & Brown, L. C. Thermal effect due to stress-induced martensite formation in β-CuAlNi single crystals. *Metall. Mater. Trans. A* **11**, 147–150 (1980).
72. Pieczyska, E. A., Tobushi, H. & Kulasinski, K. Development of transformation bands in TiNi SMA for various stress and strain rates studied by a fast and sensitive infrared camera. *Smart Mater. Struct.* **22**, 035007 (2013).
73. Wu, Y., Ertekin, E. & Sehitoglu, H. Elastocaloric cooling capacity of shape memory alloys – Role of deformation temperatures, mechanical cycling, stress hysteresis and inhomogeneity of transformation. *Acta Mater.* **135**, 158–176 (2017).
74. Cong, D. et al. Colossal elastocaloric effect in ferroelastic Ni-Mn-Ti alloys. *Phys. Rev. Lett.* **122**, 255703 (2019).
75. Frenzel, J. et al. On the effect of alloy composition on martensite start temperatures and latent heats in Ni–Ti-based shape memory alloys. *Acta Mater.* **90**, 213–231 (2015).
76. Saylor, A. 2012 ARPA-E summit technology showcase: UMD's thermoelastic cooling. *US Department of Energy* https://www.energy.gov/articles/2012-arpa-e-summit-technology-showcase (2012).
77. Qian, S. et al. in *Proceedings of the 16th International Refrigeration and Air Conditioning Conference* 2385 (Purdue Univ. Press, 2016).
78. Rodriquez, E. L. & Filisko, F. E. Thermoelastic temperature changes in poly(methyl methacrylate) at high hydrostatic pressure: experimental. *J. Appl. Phys.* **53**, 6536–6540 (1982).
79. Muller, K. A. et al. Cooling by adiabatic pressure application in $Pr_{1-x}La_xNiO_3$. *Appl. Phys. Lett.* **73**, 1056–1058 (1998).
80. Strässle, T., Furrer, A., Lacorre, P. & Müller, K. A. A novel principle for cooling by adiabatic pressure application in rare-earth compounds. *J. Alloys Compd.* **303–304**, 228–231 (2000).
81. Matsunami, D., Fujita, A., Takenaka, K. & Kano, M. Giant barocaloric effect enhanced by the frustration of the antiferromagnetic phase in $Mn_3GaN$. *Nat. Mater.* **14**, 73–78 (2015).
82. Lloveras, P. et al. Giant barocaloric effects at low pressure in ferrielectric ammonium sulphate. *Nat. Commun.* **6**, 8801 (2015).
83. Bermudez-Garcia, J. M. et al. Giant barocaloric effect in the ferroic organic-inorganic hybrid $[TPrA][Mn(dca)_3]$ perovskite under easily accessible pressures. *Nat. Commun.* **8**, 15715 (2017).
84. Kosugi, Y. et al. Colossal barocaloric effect by large latent heat produced by first-order intersite-charge-transfer transition. *Adv. Funct. Mater.* **31**, 2009476 (2021).
85. Aznar, A. et al. Giant barocaloric effects over a wide temperature range in superionic conductor AgI. *Nat. Commun.* **8**, 1851 (2017).
86. Lloveras, P. et al. Colossal barocaloric effects near room temperature in plastic crystals of neopentylglycol. *Nat. Commun.* **10**, 1803 (2019).
87. Aznar, A. et al. Reversible and irreversible colossal barocaloric effects in plastic crystals. *J. Mater. Chem. A* **8**, 639–647 (2020).
88. Aznar, A. et al. Reversible colossal barocaloric effects near room temperature in 1-X-adamantane (X=Cl, Br) plastic crystals. *Appl. Mater. Today* **23**, 101023 (2021).
89. Li, B. et al. Colossal barocaloric effects in plastic crystals. *Nature* **567**, 506–510 (2019).
90. von Ranke, P. J. et al. Colossal refrigerant capacity in $[Fe(hyptrz)_3]A_2 \cdot H_2O$ around the freezing temperature of water. *Phys. Rev. B* **98**, 224408 (2018).
91. Vallone, S. P. et al. Giant barocaloric effect at the spin crossover transition of a molecular crystal. *Adv. Mater.* **31**, 1807334 (2019).
**Experimentally examines the barocaloric effect of a molecular crystal with a pressure-driven spin-crossover transition near room temperature**.
92. Romanini, M. et al. Giant and reversible barocaloric effect in trinuclear spin-crossover complex $Fe_3(bntrz)_6(tcnset)_6$. *Adv. Mater.* **33**, 2008076 (2021).
93. Gama, S. et al. Pressure-induced colossal magnetocaloric effect in MnAs. *Phys. Rev. Lett.* **93**, 237202 (2004).
94. Morellon, L. et al. Pressure enhancement of the giant magnetocaloric effect in $Tb_5Si_2Ge_2$. *Phys. Rev. Lett.* **93**, 137201 (2004).
95. Magen, C. et al. Hydrostatic pressure control of the magnetostructural phase transition in $Gd_5Si_2Ge_2$ single crystals. *Phys. Rev. B* **72**, 024416 (2005).
96. Lyubina, J., Nenkov, K., Schultz, L. & Gutfleisch, O. Multiple metamagnetic transitions in the magnetic refrigerant $La(Fe, Si)_{13}H_x$. *Phys. Rev. Lett.* **101**, 177203 (2008).
97. de Oliveira, N. A. Entropy change upon magnetic field and pressure variations. *Appl. Phys. Lett.* **90**, 052501 (2007).
98. Planes, A., Castan, T. & Saxena, A. Thermodynamics of multicaloric effects in multiferroics. *Philos. Mag.* **94**, 1893–1908 (2014).
**Theoretically analyses the thermodynamics of multicaloric effects. The materials discussed are typical examples of category II cooling (multiple fields on single-phase materials), as defined in Fig. 2a of this Review**.
99. Liu, Y. et al. Large reversible caloric effect in FeRh thin films via a dual-stimulus multicaloric cycle. *Nat. Commun.* **7**, 11614 (2016).
100. Qiao, K. et al. Novel reduction of hysteresis loss controlled by strain memory effect in FeRh/PMN-PT heterostructures. *Nano Energy* **59**, 285–294 (2019).
**Reports a multicaloric composite, to which a magnetic field is applied to the film and an electric field to the substrate in a multistep cycle. This work is an example of category IV cooling (multiple fields on composite materials), as defined in Fig. 2a of this Review**.
101. Qiao, K. et al. Regulation of phase transition and magnetocaloric effect by ferroelectric domains in FeRh/PMN-PT heterojunctions. *Acta Mater.* **91**, 51–59 (2020).

102. Moya, X. et al. Giant and reversible extrinsic magnetocaloric effects in $La_{0.7}Ca_{0.3}MnO_3$ films due to strain. *Nat. Mater.* **12**, 52–58 (2013).
**One of the first demonstrations of multicaloric cooling in multiferroic composites and a typical example of category III cooling (single field on composite materials), as defined in Fig. 2a of this Review.**
103. Hou, H., Finkel, P., Staruch, M., Cui, J. & Takeuchi, I. Ultra-low-field magneto-elastocaloric cooling in a multiferroic composite device. *Nat. Commun.* **9**, 4075 (2018).
104. Planes, A., Castán, T. & Saxena, A. Thermodynamics of multicaloric effects in multiferroic materials: application to metamagnetic shape-memory alloys and ferrotoroidics. *Phil. Trans. R. Soc. A* **374**, 20150304 (2016).
105. Pecharsky, V. K. & Gschneidner, K. A. $Gd_5(Si_xGe_{1-x})_4$: an extremum material. *Adv. Mater.* **13**, 683–686 (2001).
106. Gschneidner, K. A., Pecharsky, V. K. & Tsokol, A. O. Recent developments in magnetocaloric materials. *Rep. Prog. Phys.* **68**, 1479–1539 (2005).
107. Yuce, S. et al. Barocaloric effect in the magnetocaloric prototype $Gd_5Si_2Ge_2$. *Appl. Phys. Lett.* **101**, 071906 (2012).
108. Grăcia-Condal, A. et al. Multicaloric effects in metamagnetic Heusler Ni-Mn-In under uniaxial stress and magnetic field. *Appl. Phys. Rev.* **7**, 041406 (2020).
**Demonstrates the multicaloric effect of Ni–Mn–In Heusler alloys under a magnetic field and uniaxial stress. Provides another example of category II cooling (multiple fields on single-phase materials), as defined in Fig. 2a of this Review.**
109. Czernuszewicz, A., Kaleta, J. & Lewandowski, D. Multicaloric effect: toward a breakthrough in cooling technology. *Energy Convers. Manag.* **178**, 335–342 (2018).
110. Soto-Parra, D. E. et al. Stress- and magnetic field-induced entropy changes in Fe-doped Ni–Mn–Ga shape-memory alloys. *Appl. Phys. Lett.* **96**, 071912 (2010).
111. Castillo-Villa, P. O. et al. Elastocaloric and magnetocaloric effects in Ni-Mn-Sn(Cu) shape-memory alloy. *J. Appl. Phys.* **113**, 053506 (2013).
112. Matsunami, D. & Fujita, A. Electrocaloric effect of metal-insulator transition in $VO_2$. *Appl. Phys. Lett.* **106**, 042901 (2015).
113. Ouyang, G. et al. Elastocaloric effect in vanadium (IV) oxide. *Appl. Phys. Lett.* **116**, 251901 (2020).
114. Park, J. H. et al. Measurement of a solid-state triple point at the metal–insulator transition in $VO_2$. *Nature* **500**, 431–434 (2013).
115. Prah, U., Wencka, M., Rojac, T., Benčan, A. & Uršič, H. $Pb(Fe_{0.5}Nb_{0.5})O_3$–$BiFeO_3$-based multicalorics with room-temperature ferroic anomalies. *J. Mater. Chem. C* **8**, 11282–11291 (2020).
116. Starkov, I. A. & Starkov, A. S. On the thermodynamic foundations of solid-state cooler based on multiferroic materials. *Int. J. Refrig.* **37**, 249–256 (2014).
117. Zhao, Y.-Q. & Cao, H.-X. Multicaloric effect in multiferroic $EuTiO_3$ thin films. *J. Mater. Sci.* **55**, 5705–5714 (2020).
118. van Erp, R., Soleimanzadeh, R., Nela, L., Kampitsis, G. & Matioli, E. Co-designing electronics with microfluidics for more sustainable cooling. *Nature* **585**, 211–216 (2020).
119. Amirov, A. A., Rodionov, V. V., Starkov, I. A., Starkov, A. S. & Aliev, A. M. Magneto-electric coupling in $Fe_{48}Rh_{52}$-PZT multiferroic composite. *J. Magn. Magn. Mater.* **470**, 77–80 (2019).
120. Andrade, V. M. et al. Multicaloric effect in a multiferroic composite of $Gd_5(Si,Ge)_4$ microparticles embedded into a ferroelectric PVDF matrix. *Sci. Rep.* **9**, 18308 (2019).
121. Gottschall, T. et al. A multicaloric cooling cycle that exploits thermal hysteresis. *Nat. Mater.* **17**, 929–934 (2018).
**Reports the use of two stimuli — a magnetic field and uniaxial stress — that are applied sequentially to a multicaloric material to exploit the hysteresis. Provides another example of category II cooling (multiple fields on single-phase materials), as defined in Fig. 2a of this Review.**
122. Mañosa, L. & Planes, A. Solid-state cooling by stress: a perspective. *Appl. Phys. Lett.* **116**, 050501 (2020).
123. Hou, H. et al. Overcoming fatigue through compression for advanced elastocaloric cooling. *MRS Bull.* **43**, 285–290 (2018).
124. Sebald, G., Komiya, A., Jay, J., Coativy, G. & Lebrun, L. Regenerative cooling using elastocaloric rubber: analytical model and experiments. *J. Appl. Phys.* **127**, 094903 (2020).
125. Guyomar, D. et al. Elastocaloric modeling of natural rubber. *Appl. Therm. Eng.* **57**, 33–38 (2013).
126. Xie, Z. J., Sebald, G. & Guyomar, D. Comparison of elastocaloric effect of natural rubber with other caloric effects on different-scale cooling application cases. *Appl. Therm. Eng.* **111**, 914–926 (2017).
127. Chauhan, A., Patel, S. & Vaish, R. Elastocaloric effect in ferroelectric ceramics. *Appl. Phys. Lett.* **106**, 172901 (2015).
128. Patel, S., Chauhan, A. & Vaish, R. Elastocaloric and piezocaloric effects in lead zirconate titanate ceramics. *Energy Technol.* **4**, 647–652 (2016).
129. Christian, J. W. *The Theory of Transformations in Metals and Alloys* (Pergamon, 2002).
130. Bhadeshia, H. K. D. H. *Worked examples in the Geometry of Crystals* (Institute of Materials, 2001).
131. Lagoudas, D. C. *Shape Memory Alloys: Modeling and Engineering Applications* (Springer, 2008).
132. Wang, R. et al. Torsional refrigeration by twisted, coiled, and supercoiled fibers. *Science* **366**, 216–221 (2019).
133. Wang, R., Zhou, X., Wang, W. & Liu, Z. Twist-based cooling of polyvinylidene difluoride for mechanothermochromic fibers. *Chem. Eng. J.* **417**, 128060 (2020).
134. Sharar, D. J., Radice, J., Warzoha, R., Hanrahan, B. & Smith, A. Low-force elastocaloric refrigeration via bending. *Appl. Phys. Lett.* **118**, 184103 (2021).
135. Czernuszewicz, A., Griffith, L., Slaughter, J. & Pecharsky, V. Low-force compressive and tensile actuation for elastocaloric heat pumps. *Appl. Mater. Today* **19**, 100557 (2020).
136. Slaughter, J., Czernuszewicz, A., Griffith, L. & Pecharsky, V. Compact and efficient elastocaloric heat pumps — Is there a path forward? *J. Appl. Phys.* **127**, 194501 (2020).
137. Czernuszewicz, A., Griffith, L., Scott, A., Slaughter, J. & Pecharsky, V. Unlocking large compressive strains in thin active elastocaloric layers. *Appl. Therm. Eng.* **190**, 116850 (2021).
138. Khassaf, H., Patel, T., Hebert, R. J. & Alpay, S. P. Flexocaloric response of epitaxial ferroelectric films. *J. Appl. Phys.* **123**, 024102 (2018).
139. Ikeda, M. S. et al. Elastocaloric signature of nematic fluctuations. *Proc. Natl Acad. Sci. USA* **118**, e2105911118 (2021).
140. Sanchez, J. J. et al. The transport–structural correspondence across the nematic phase transition probed by elasto X-ray diffraction. *Nat. Mater.* **20**, 1519–1524 (2021).
141. Cui, J. et al. Combinatorial search of thermoelastic shape-memory alloys with extremely small hysteresis width. *Nat. Mater.* **5**, 286–290 (2006).
142. Provenzano, V., Shapiro, A. J. & Shull, R. D. Reduction of hysteresis losses in the magnetic refrigerant $Gd_5Ge_2Si_2$ by the addition of iron. *Nature* **429**, 853–857 (2004).
143. Guillou, F., Porcari, G., Yibole, H., van Dijk, N. & Bruck, E. Taming the first-order transition in giant magnetocaloric materials. *Adv. Mater.* **26**, 2671–2675 (2014).
144. Fulanovic, L. et al. Fatigue-less electrocaloric effect in relaxor $Pb(Mg_{1/3}Nb_{2/3})O_3$ multilayer elements. *J. Eur. Ceram. Soc.* **37**, 5105–5108 (2017).
145. Masche, M., Ianniciello, L., Tušek, J. & Engelbrecht, K. Impact of hysteresis on caloric cooling performance. *Int. J. Refrig.* **121**, 302–312 (2021).
146. Hess, T. et al. Thermal hysteresis and its impact on the efficiency of first-order caloric materials. *J. Appl. Phys.* **127**, 075103 (2020).
147. Rowe, A. Thermal effectiveness of active caloric regenerators. *J. Appl. Phys.* **127**, 204502 (2020).
148. Govindappa, P. et al. Predicting the thermal hysteresis behavior for a single-layer $MnFeP_{1-x}Si_x$ active magnetic regenerator. *Appl. Therm. Eng.* **183**, 116173 (2021).
149. Hamilton, R. F., Sehitoglu, H., Chumlyakov, Y. & Maier, H. J. Stress dependence of the hysteresis in single crystal NiTi alloys. *Acta Mater.* **52**, 3383–3402 (2004).
150. Ortin, J. & Planes, A. Thermodynamic analysis of thermal measurements in thermoelastic martensitic transformations. *Acta Metall.* **36**, 1873–1889 (1988).
151. Callister, W. D. & Rethwisch, D. G. *Materials Science and Engineering: An Introduction* Ch. 20 (Wiley, 2007).
152. Gutfleisch, O. et al. Mastering hysteresis in magnetocaloric materials. *Phil. Trans. R. Soc. A* **374**, 20150308 (2016).
153. Marathe, M., Ederer, C. & Grunebohm, A. The impact of hysteresis on the electrocaloric effect at first-order phase transitions. *Phys. Status Solidi B* **255**, 1700308 (2018).
154. Scheibel, F. et al. Hysteresis design of magnetocaloric materials — from basic mechanisms to applications. *Energy Technol.* **6**, 1397–1428 (2018).
155. Ball, J. M. & James, R. D. Proposed experimental tests of a theory of fine microstructure and the two-well problem. *Phil. Trans. R. Soc. A* **338**, 389–450 (1992).
156. Chen, X., Srivastava, V., Dabade, V. & James, R. D. Study of the cofactor conditions: conditions of supercompatibility between phases. *J. Mech. Phys. Solids* **61**, 2566–2587 (2013).
157. Song, Y., Chen, X., Dabade, V., Shield, T. W. & James, R. D. Enhanced reversibility and unusual microstructure of a phase-transforming material. *Nature* **502**, 85–88 (2013).
158. Gu, H. et al. Exploding and weeping ceramics. *Nature* **599**, 416–420 (2021).
159. Fujieda, S., Fukamichi, K. & Suzuki, S. Suppression of aqueous corrosion of $La(Fe_{0.88}Si_{0.12})_{13}$ by reducing dissolved oxygen concentration for high-performance magnetic refrigeration. *J. Alloys Compd.* **600**, 67–70 (2014).
160. Forchelet, J. et al. Corrosion behavior of gadolinium and La–Fe–Co–Si compounds in various heat conducting fluids. *Int. J. Refrig.* **37**, 307–313 (2014).
161. Balli, M., Jandl, S., Fournier, P. & Kedous-Lebouc, A. Advanced materials for magnetic cooling: fundamentals and practical aspects. *Appl. Phys. Rev.* **4**, 021305 (2017).
162. Guillou, F. et al. Non-hysteretic first-order phase transition with large latent heat and giant low-field magnetocaloric effect. *Nat. Commun.* **9**, 2925 (2018).
163. San Juan, J., No, M. L. & Schuh, C. A. Nanoscale shape-memory alloys for ultrahigh mechanical damping. *Nat. Nanotechnol.* **4**, 415–419 (2009).
164. Chen, Y. & Schuh, C. A. Size effects in shape memory alloy microwires. *Acta Mater.* **59**, 537–553 (2011).
165. Otsuka, K. & Wayman, C. M. *Shape Memory Materials* (Cambridge Univ. Press, 1998).
166. Sehitoglu, H., Patriarca, L. & Wu, Y. Shape memory strains and temperatures in the extreme. *Curr. Opin. Solid State Mater. Sci.* **21**, 113–120 (2017).
167. Ashby, M. F., Shercliff, H. & Cebon, D. *Materials: Engineering, Science, Processing and Design* Ch. 9 (Butterworth-Heinemann, 2007).
168. Bradesko, A. et al. Electrocaloric fatigue of lead magnesium niobate mediated by an electric-field-induced phase transformation. *Acta Mater.* **169**, 275–283 (2019).
169. Duca, M. G. D. et al. Comprehensive evaluation of electrocaloric effect and fatigue behavior in the $0.9Pb(Mg_{1/3}Nb_{2/3})O_3$–$0.1PbTiO_3$ bulk relaxor ferroelectric ceramic. *J. Appl. Phys.* **128**, 104102 (2020).
170. Weyland, F. et al. Long term stability of electrocaloric response in barium zirconate titanate. *J. Eur. Ceram. Soc.* **38**, 551–556 (2018).
171. Moore, J. D. et al. Selective laser melting of $La(Fe,Co,Si)_{13}$ geometries for magnetic refrigeration. *J. Appl. Phys.* **114**, 043907 (2013).
172. Lyubina, J., Schafer, R., Martin, N., Schultz, L. & Gutfleisch, O. Novel design of $La(Fe, Si)_{13}$ alloys towards high magnetic refrigeration performance. *Adv. Mater.* **22**, 3735–3739 (2010).
173. Yibole, H. et al. Moment evolution across the ferromagnetic phase transition of giant magnetocaloric $(Mn, Fe)_2(P, Si, B)$ compounds. *Phys. Rev. B* **91**, 014429 (2015).
174. Liu, Y., Fu, X., Yu, Q., Zhang, M. & Liu, J. Significant reduction of phase-transition hysteresis for magnetocaloric $(La_{1-x}Ce_x)_2Fe_{11}Si_2Hy$ alloys by microstructural manipulation. *Acta Mater.* **207**, 116687 (2021).
175. Bai, Y., Han, X., Zheng, X. C. & Qiao, L. J. Both high reliability and giant electrocaloric strength in $BaTiO_3$ ceramics. *Sci. Rep.* **3**, 2895 (2013).
176. Katter, M., Zellmann, V., Reppel, G. W. & Uestuener, K. Magnetocaloric properties of $La(FeCoSi)_{13}$ bulk material prepared by powder metallurgy. *IEEE Trans. Magn.* **44**, 3044–3047 (2008).
177. Chauhan, A., Patel, S. & Vaish, R. Multicaloric effect in $Pb(Mn_{1/3}Nb_{2/3})O_3$-$32PbTiO_3$ single crystals. *Acta Mater.* **9**, 384–395 (2015).
178. Chauhan, A., Patel, S. & Vaish, R. Multicaloric effect in $Pb(Mn_{1/3}Nb_{2/3})O_3$-$32PbTiO_3$ single crystals: modes of measurement. *Acta Mater.* **97**, 17–28 (2015).
179. Hu, Y. et al. Combined caloric effects in a multiferroic Ni–Mn–Ga alloy with broad refrigeration temperature region. *APL Mater.* **5**, 046103 (2017).
180. Li, Z. et al. Achieving a broad refrigeration temperature region through the combination of

successive caloric effects in a multiferroic $Ni_{50}Mn_{35}In_{15}$ alloy. *Acta Mater.* **192**, 52–59 (2020).
181. Stern-Taulats, E. et al. Giant multicaloric response of bulk $Fe_{49}Rh_{51}$. *Phys. Rev. B* **95**, 104424 (2017).
182. Grācia-Condal, A., Stern-Taulats, E., Planes, A. & Mañosa, L. Caloric response of $Fe_{49}Rh_{51}$ subjected to uniaxial load and magnetic field. *Phys. Rev. Mater.* **2**, 084413 (2018).
183. Odaira, T., Xu, S., Xu, X., Omori, T. & Kainuma, R. Elastocaloric switching effect induced by reentrant martensitic transformation. *Appl. Phys. Rev.* **7**, 031406 (2020).
184. Gottschall, T. et al. Advanced characterization of multicaloric materials in pulsed magnetic fields. *J. Appl. Phys.* **127**, 185107 (2020).
185. BASF. Premiere of cutting-edge cooling appliance at CES 2015. BASF Joint News Release https://www.basf.com/global/en/media/news-releases/2015/01/p-15-100.html (2015).
186. Nakashima, A. T. D. et al. A magnetic wine cooler prototype. *Int. J. Refrig.* **122**, 110–121 (2021).
187. Lionte, S., Risser, M. & Muller, C. A 15 kW magnetocaloric proof-of-concept unit: initial development and first experimental results. *Int. J. Refrig.* **122**, 256–265 (2021).
188. Trevizoli, P. V., Nakashima, A. T., Peixer, G. F. & Barbosa, J. R. Performance evaluation of an active magnetic regenerator for cooling applications — part I: experimental analysis and thermodynamic performance. *Int. J. Refrig.* **72**, 192–205 (2016).
189. Aprea, C., Cardillo, G., Greco, A., Maiorino, A. & Masselli, C. A rotary permanent magnet magnetic refrigerator based on AMR cycle. *Appl. Therm. Eng.* **101**, 699–703 (2016).
190. Cheng, P. et al. Combining magnetocaloric and elastocaloric effects in a $Ni_{45}Co_5Mn_{37}In_{13}$ alloy. *J. Mater. Sci. Technol.* **94**, 47–52 (2021).
191. Qian, S. et al. Not-in-kind cooling technologies: a quantitative comparison of refrigerants and system performance. *Int. J. Refrig.* **62**, 177–192 (2016). **Analyses and visualizes $COP_{mat}$ for single-phase caloric materials**.
192. Zimm, C. et al. in *Advances in Cryogenic Engineering* (ed. Kittel, P.) 1759–1766 (Springer, 1998).
193. Pecharsky, V. K. & Gschneidner, K. A. Magnetocaloric effect and magnetic refrigeration. *J. Magn. Magn. Mater.* **200**, 44–56 (1999).
194. Steyert, W. Stirling-cycle rotating magnetic refrigerators and heat engines for use near room temperature. *J. Appl. Phys.* **49**, 1216–1226 (1978).
195. Barclay, J. A. & Steyert, W. A. Active magnetic regenerator. US Patent 4,332,135 (1982).
196. Sinyavsky, Y. V. & Brodyansky, V. M. Experimental testing of electrocaloric cooling with transparent ferroelectric ceramic as a working body. *Ferroelectrics* **131**, 321–325 (1992).
197. Gu, H. et al. A chip scale electrocaloric effect based cooling device. *Appl. Phys. Lett.* **102**, 122904 (2013).
198. McLinden, M. O., Brown, J. S., Brignoli, R., Kazakov, A. F. & Domanski, P. A. Limited options for low-global-warming-potential refrigerants. *Nat. Commun.* **8**, 14476 (2017).
199. McLinden, M. O., Seeton, C. J. & Pearson, A. New refrigerants and system configurations for vapor-compression refrigeration. *Science* **370**, 791–796 (2020).
200. Hou, H. et al. Elastocaloric cooling of additive manufactured shape memory alloys with large latent heat. *J. Phys. D* **50**, 404001 (2017).
201. McLinden, M. O. in *ASHRAE Handbook — Fundamentals* (ed. Owen, M. S.) 749–826 (ASHRAE, 2017).
202. Hou, H., Takeuchi, I., Staruch, M. & Finkel, P. Systems and methods for cooling using a composite elastocaloric device. US Patent application 2020096240-A1 (2020).
203. Stacey, W. C. & Litt, B. Technology insight: neuroengineering and epilepsy - designing devices for seizure control. *Nat. Rev. Neurol.* **4**, 190–201 (2008).
204. Smyth, M. D. & Rothman, S. M. Focal cooling devices for the surgical treatment of epilepsy. *Neurosurg. Clin.* **22**, 533–546 (2011).
205. Smyth, M. D. et al. Temperatures achieved in human and canine neocortex during intraoperative passive or active focal cooling. *Ther. Hypothermia Temp. Manag.* **5**, 95–103 (2015).
206. Musk, E. An integrated brain-machine interface platform with thousands of channels. *J. Med. Internet Res.* **21**, e16194 (2019).
207. Numazawa, T., Kamiya, K., Utaki, T. & Matsumoto, K. Magnetic refrigerator for hydrogen liquefaction. *Cryogenics* **62**, 185–192 (2014).
208. Kim, Y., Park, I. & Jeong, S. Experimental investigation of two-stage active magnetic regenerative refrigerator operating between 77 K and 20 K. *Cryogenics* **57**, 113–121 (2013).
209. Park, I. & Jeong, S. Development of the active magnetic regenerative refrigerator operating between 77 K and 20 K with the conduction cooled high temperature superconducting magnet. *Cryogenics* **88**, 106–115 (2017).
210. Holladay, J. et al. Investigation of bypass fluid flow in an active magnetic regenerative liquefier. *Cryogenics* **93**, 34–40 (2018).
211. Teyber, R. et al. Passive force balancing of an active magnetic regenerative liquefier. *J. Magn. Magn. Mater.* **451**, 79–86 (2018).
212. Teyber, R. et al. Performance investigation of a high-field active magnetic regenerator. *Appl. Energy* **236**, 426–436 (2019).
213. DebRoy, T. et al. Additive manufacturing of metallic components - Process, structure and properties. *Prog. Mater. Sci.* **92**, 112–224 (2018).
214. Frazier, W. E. Metal additive manufacturing: a review. *J. Mater. Eng. Perform.* **23**, 1917–1928 (2014).
215. DebRoy, T., Mukherjee, T., Wei, H. L., Elmer, J. W. & Milewski, J. O. Metallurgy, mechanistic models and machine learning in metal printing. *Nat. Rev. Mater.* **6**, 48–68 (2021).
216. Navickaitė, K. et al. Experimental characterization of active magnetic regenerators constructed using laser beam melting technique. *Appl. Therm. Eng.* **174**, 115297 (2020).
217. Lejeune, B. T. et al. Towards additive manufacturing of magnetocaloric working materials. *Materialia* **16**, 101071 (2021).
218. Tabor, D. P. et al. Accelerating the discovery of materials for clean energy in the era of smart automation. *Nat. Rev. Mater.* **3**, 5–20 (2018).
219. Kusne, A. G. et al. On-the-fly closed-loop materials discovery via Bayesian active learning. *Nat. Commun.* **11**, 5966 (2020).
220. Zhu, Z., Ng, D. W. H., Park, H. S. & McAlpine, M. C. 3D-printed multifunctional materials enabled by artificial-intelligence-assisted fabrication technologies. *Nat. Rev. Mater.* **6**, 27–47 (2021).
221. Klinar, K. & Kitanovski, A. Thermal control elements for caloric energy conversion. *Renew. Sust. Energ. Rev.* **118**, 109571 (2020).
222. Klinar, K., Swoboda, T., Muñoz Rojo, M. & Kitanovski, A. Fluidic and mechanical thermal control devices. *Adv. Electron. Mater.* **7**, 2000623 (2020). **Comprehensive analysis of state-of-the-art thermal control devices, whose implementation in applications spans different sizes and temperatures**.
223. Maier, L. M. et al. Active magnetocaloric heat pipes provide enhanced specific power of caloric refrigeration. *Commun. Phys.* **3**, 186 (2020).
224. Welty, J. R., Wicks, C. E., Wilson, R. E. & Rorrer, G. L. *Fundamentals of Momentum, Heat, and Mass Transfer* (Wiley, 2007).
225. Hess, T. et al. Modelling cascaded caloric refrigeration systems that are based on thermal diodes or switches. *Int. J. Refrig.* **103**, 215–222 (2019).
226. Porenta, L. et al. Thin-walled Ni-Ti tubes under compression: ideal candidates for efficient and fatigue-resistant elastocaloric cooling. *Appl. Mater. Today* **20**, 100712 (2020).
227. Ding, L. et al. Learning from superelasticity data to search for Ti-Ni alloys with large elastocaloric effect. *Acta Mater.* **218**, 117200 (2021).
228. Bom, N. M., Usuda, E. O., Guimaraes, G. M., Coelho, A. A. & Carvalho, A. M. G. Note: Experimental setup for measuring the barocaloric effect in polymers: application to natural rubber. *Rev. Sci. Instrum.* **88**, 046103 (2017).
229. Usuda, E. O., Imamura, W., Bom, N. M., Paixão, L. S. & Carvalho, A. M. G. Giant reversible barocaloric effects in nitrile butadiene rubber around room temperature. *ACS Appl. Polym. Mater.* **1**, 1991–1997 (2019).
230. Giguère, A. et al. Direct measurement of the "giant" adiabatic temperature change in $Gd_5Si_2Ge_2$. *Phys. Rev. Lett.* **83**, 2262–2265 (1999).
231. Chirkova, A. et al. Giant adiabatic temperature change in FeRh alloys evidenced by direct measurements under cyclic conditions. *Acta Mater.* **106**, 15–21 (2016).
232. Annaorazov, M. P. et al. Alloys of the Fe–Rh system as a new class of working material for magnetic refrigerators. *Cryogenics* **32**, 867–872 (1992).
233. Dan'Kov, S. Y., Tishin, A., Pecharsky, V. & Gschneidner, K. Magnetic phase transitions and the magnetothermal properties of gadolinium. *Phys. Rev. B* **57**, 3478 (1998).
234. Gottschall, T. et al. Magnetocaloric effect of gadolinium in high magnetic fields. *Phys. Rev. B* **99**, 134429 (2019).
235. Kihara, T., Kohama, Y., Hashimoto, Y., Katsumoto, S. & Tokunaga, M. Adiabatic measurements of magneto-caloric effects in pulsed high magnetic fields up to 55 T. *Rev. Sci. Instrum.* **84**, 074901 (2013).
236. Zavareh, M. G. et al. Direct measurement of the magnetocaloric effect in $La(Fe,Si,Co)_{13}$ compounds in pulsed magnetic fields. *Phys. Rev. Appl.* **8**, 014037 (2017).
237. Tuttle, B. A. & Payne, D. A. The effects of microstructure on the electrocaloric properties of $Pb(Zr,Sn,Ti)O_3$ ceramics. *Ferroelectrics* **37**, 603–606 (1981).
238. Rožič, B. et al. Influence of the critical point on the electrocaloric response of relaxor ferroelectrics. *J. Appl. Phys.* **110**, 064118 (2011).
239. Rožič, B. et al. Direct measurements of the giant electrocaloric effect in soft and solid ferroelectric materials. *Ferroelectrics* **405**, 26–31 (2010).
240. Zheng, X.-C., Zheng, G.-P., Lin, Z. & Jiang, Z.-Y. Electro-caloric behaviors of lead-free $Bi_{0.5}Na_{0.5}TiO_3$-$BaTiO_3$ ceramics. *J. Electroceramics* **28**, 20–26 (2012).
241. Lu, S. G. et al. Comparison of directly and indirectly measured electrocaloric effect in relaxor ferroelectric polymers. *Appl. Phys. Lett.* **97**, 202901 (2010).
242. Nouchokgwe, Y. et al. Giant electrocaloric materials energy efficiency in highly ordered lead scandium tantalate. *Nat. Commun.* **12**, 3298 (2021).
243. Wang, S. et al. Direct and indirect measurement of large electrocaloric effect in $B_2O_3$-ZnO glass modified $Ba_{0.65}Sr_{0.35}TiO_3$ bulk ceramics. *Scr. Mater.* **193**, 59–63 (2021).
244. Lu, S. G., Rožič, B., Zhang, Q. M., Kutnjak, Z. & Neese, B. Enhanced electrocaloric effect in ferroelectric poly(vinylidene-fluoride/trifluoroethylene) 55/45 mol% copolymer at ferroelectric-paraelectric transition. *Appl. Phys. Lett.* **98**, 122906 (2011).
245. Lu, S. G. et al. Organic and inorganic relaxor ferroelectrics with giant electrocaloric effect. *Appl. Phys. Lett.* **97**, 162904 (2010).
246. Pataky, G. J., Ertekin, E. & Sehitoglu, H. Elastocaloric cooling potential of NiTi, $Ni_2FeGa$, and CoNiAl. *Acta Mater.* **96**, 420–427 (2015).
247. Soto-Parra, D. et al. Elastocaloric effect in Ti-Ni shape-memory wires associated with the B2↔B19′ and B2↔R structural transitions. *Appl. Phys. Lett.* **108**, 071902 (2016).
248. Trung, N. T., Zhang, L., Caron, L., Buschow, K. H. J. & Brück, E. Giant magnetocaloric effects by tailoring the phase transitions. *Appl. Phys. Lett.* **96**, 172504 (2010).
249. Wada, H. & Tanabe, Y. Giant magnetocaloric effect of $MnAs_{1-x}Sb_x$. *Appl. Phys. Lett.* **79**, 3302–3304 (2001).
250. Hu, F. X. et al. Large magnetic entropy change with small thermal hysteresis near room temperature in metamagnetic alloys $Ni_{51}Mn_{49-x}In_x$. *J. Appl. Phys.* **105**, 07A940 (2009).
251. Samanta, T. et al. Hydrostatic pressure-induced modifications of structural transitions lead to large enhancements of magnetocaloric effects in MnNiSi-based systems. *Phys. Rev. B* **91**, 020401 (2015).
252. Clifford, D., Sharma, V., Deepak, K., Ramanujan, R. V. & Barua, R. Multicaloric effects in $(MnNiSi)_{1-x}(Fe_2Ge)_x$ alloys. *IEEE Trans. Magn.* **57**, 2500405 (2021).
253. Samanta, T. et al. Barocaloric and magnetocaloric effects in $(MnNiSi)_{1-x}(FeCoGe)_x$. *Appl. Phys. Lett.* **112**, 021907 (2018).
254. Liu, X. Q., Chen, T. T., Wu, Y. J. & Chen, X. M. Enhanced electrocaloric effects in spark plasma-sintered $Ba_{0.65}Sr_{0.35}TiO_3$-based ceramics at room temperature. *J. Am. Ceram. Soc.* **96**, 1021–1023 (2013).
255. Crossley, S., Nair, B., Whatmore, R. W., Moya, X. & Mathur, N. D. Electrocaloric cooling cycles in lead scandium tantalate with true regeneration via field variation. *Phys. Rev. X* **9**, 041002 (2019).
256. Qian, X. S. et al. Giant electrocaloric response over a broad temperature range in modified $BaTiO_3$ ceramics. *Adv. Funct. Mater.* **24**, 1300–1305 (2014).
257. Li, X. et al. Giant electrocaloric effect in ferroelectric poly(vinylidenefluoride-trifluoroethylene) copolymers near a first-order ferroelectric transition. *Appl. Phys. Lett.* **101**, 132903 (2012).
258. Mañosa, L., Jarque-Farnos, S., Vives, E. & Planes, A. Large temperature span and giant refrigerant capacity

in elastocaloric Cu-Zn-Al shape memory alloys. *Appl. Phys. Lett.* **103**, 211904 (2013).
259. Stern-Taulats, E. et al. Tailoring barocaloric and magnetocaloric properties in low-hysteresis magnetic shape memory alloys. *Acta Mater.* **96**, 324–332 (2015).
260. Shen, J., Wu, J. F. & Sun, J. R. Room-temperature large refrigerant capacity of $Gd_5Co_2Si_3$. *J. Appl. Phys.* **106**, 083902 (2009).
261. Li, L. W., Niehaus, O., Kersting, M. & Pottgen, R. Reversible table-like magnetocaloric effect in $Eu_4PdMg$ over a very large temperature span. *Appl. Phys. Lett.* **104**, 092416 (2014).
262. Moreira, R. L. Electrocaloric effect in γ-irradiated P(VDF-TrFE) copolymers with relaxor features. *Ferroelectrics* **446**, 1–8 (2013).
263. Correia, T. M. et al. PST thin films for electrocaloric coolers. *J. Phys. D* **44**, 165407 (2011).
264. Tušek, J., Kitanovski, A., Tomc, U., Favero, C. & Poredoš, A. Experimental comparison of multi-layered La–Fe–Co–Si and single-layered Gd active magnetic regenerators for use in a room-temperature magnetic refrigerator. *Int. J. Refrig.* **37**, 117–126 (2014).
265. Legait, U., Guillou, F., Kedous-Lebouc, A., Hardy, V. & Almanza, M. An experimental comparison of four magnetocaloric regenerators using three different materials. *Int. J. Refrig.* **37**, 147–155 (2014).
266. Chirkova, A. et al. The effect of the microstructure on the antiferromagnetic to ferromagnetic transition in FeRh alloys. *Acta Mater.* **131**, 31–38 (2017).
267. Li, Q. et al. Relaxor ferroelectric-based electrocaloric polymer nanocomposites with a broad operating temperature range and high cooling energy. *Adv. Mater.* **27**, 2236–2241 (2015).
268. Zhao, C., Yang, J., Huang, Y., Hao, X. & Wu, J. Broad-temperature-span and large electrocaloric effect in lead-free ceramics utilizing successive and metastable phase transitions. *J. Mater. Chem. A* **7**, 25526–25536 (2019).
269. Zarnetta, R. et al. Identification of quaternary shape memory alloys with near-zero thermal hysteresis and unprecedented functional stability. *Adv. Funct. Mater.* **20**, 1917–1923 (2010).
270. Chluba, C. et al. Ultralow-fatigue shape memory alloy films. *Science* **348**, 1004–1007 (2015).
271. Chen, H. et al. Unprecedented non-hysteretic superelasticity of [001]-oriented NiCoFeGa single crystals. *Nat. Mater.* **19**, 712–718 (2020).
272. Hao, S. et al. A transforming metal nanocomposite with large elastic strain, low modulus, and high strength. *Science* **339**, 1191–1194 (2013).
273. Moya, X. et al. Giant electrocaloric strength in single-crystal $BaTiO_3$. *Adv. Mater.* **25**, 1360–1365 (2013).
274. Weyland, F. et al. Impact of polarization dynamics and charged defects on the electrocaloric response of ferroelectric $Pb(Zr,Ti)O_3$ ceramics. *Energy Technol.* **6**, 1519–1525 (2018).
275. Zhang, K., Kang, G. & Sun, Q. High fatigue life and cooling efficiency of NiTi shape memory alloy under cyclic compression. *Scr. Mater.* **159**, 62–67 (2019).
276. Chen, J., Zhang, K., Kan, Q., Yin, H. & Sun, Q. Ultra-high fatigue life of NiTi cylinders for compression-based elastocaloric cooling. *Appl. Phys. Lett.* **115**, 093902 (2019).
277. Hua, P., Xia, M., Onuki, Y. & Sun, Q. Nanocomposite NiTi shape memory alloy with high strength and fatigue resistance. *Nat. Nanotechnol.* **16**, 409–413 (2021).
278. Xiao, F., Bucsek, A., Jin, X., Porta, M. & Planes, A. Giant elastic response and ultra-stable elastocaloric effect in tweed textured Fe-Pd single crystals. *Acta Mater.* **223**, 117486 (2022).
279. Pulko, B. et al. Epoxy-bonded La–Fe–Co–Si magnetocaloric plates. *J. Magn. Magn. Mater.* **375**, 65–73 (2015).
280. Bruederlin, F., Ossmer, H., Wendler, F., Miyazaki, S. & Kohl, M. SMA foil-based elastocaloric cooling: from material behavior to device engineering. *J. Phys. D* **50**, 424003 (2017).
281. Snodgrass, R. & Erickson, D. A multistage elastocaloric refrigerator and heat pump with 28 K temperature span. *Sci. Rep.* **9**, 18532 (2019).
282. Qian, S., Yuan, L., Hou, H. & Takeuchi, I. Accurate prediction of work and coefficient of performance of elastocaloric materials with phase transformation kinetics. *Sci. Technol. Built Environ.* **24**, 673–684 (2018).
283. Bahl, C. R. H. et al. Development and experimental results from a 1 kW prototype AMR. *Int. J. Refrig.* **37**, 78–83 (2014).
284. Liang, J. et al. Performance assessment of a triangular microchannel active magnetic regenerator. *Appl. Therm. Eng.* **186**, 116519 (2021).
285. Benedict, M. A., Sherif, S. A., Beers, D. G. & Schroeder, M. G. Design and performance of a novel magnetocaloric heat pump. *Sci. Technol. Built Environ.* **22**, 520–526 (2016).
286. Lozano, J. A. et al. Development of a novel rotary magnetic refrigerator. *Int. J. Refrig.* **68**, 187–197 (2016).
287. Zhang, T., Qian, X. S., Gu, H. M., Hou, Y. & Zhang, Q. M. An electrocaloric refrigerator with direct solid to solid regeneration. *Appl. Phys. Lett.* **110**, 243503 (2017).
288. Liu, X. et al. Giant room temperature electrocaloric effect in a layered hybrid perovskite ferroelectric: $[(CH_3)_2CHCH_2NH_3]_2PbCl_4$. *Nat. Commun.* **12**, 5502 (2021).
289. Qian, X. et al. High-entropy polymer produces a giant electrocaloric effect at low fields. *Nature* **600**, 664–669 (2021).
290. Bachmann, N. et al. Long-term stable compressive elastocaloric cooling system with latent heat transfer. *Commun. Phys.* **4**, 194 (2021).
291. Engelbrecht, K. et al. A regenerative elastocaloric device: experimental results. *J. Phys. D* **50**, 424006 (2017).
292. Bruederlin, F. et al. Elastocaloric cooling on the miniature scale: a review on materials and device engineering. *Energy Technol.* **6**, 1588–1604 (2018).
293. Saito, A. T., Kobayashi, T., Kaji, S., Li, J. & Nakagome, H. Environmentally friendly magnetic refrigeration technology using ferromagnetic Gd alloys. *Int. J. Environ. Sci. Dev.* **7**, 316–320 (2016).
294. Arnold, D. S., Tura, A., Ruebsaat-Trott, A. & Rowe, A. Design improvements of a permanent magnet active magnetic refrigerator. *Int. J. Refrig.* **37**, 99–105 (2014).
295. Yao, G. H., Gong, M. Q. & Wu, J. F. Experimental study on the performance of a room temperature magnetic refrigerator using permanent magnets. *Int. J. Refrig.* **29**, 1267–1273 (2006).
296. Greibich, F. et al. Elastocaloric heat pump with specific cooling power of 20.9 W $g^{-1}$ exploiting snap-through instability and strain-induced crystallization. *Nat. Energy* **6**, 260–267 (2021).
297. Ianniciello, L., Bartholomé, K., Fitger, A. & Engelbrecht, K. Long life elastocaloric regenerator operating under compression. *Appl. Therm. Eng.* **202**, 117838 (2022).
298. Huang, B. et al. Development of an experimental rotary magnetic refrigerator prototype. *Int. J. Refrig.* **104**, 42–50 (2019).
299. Eriksen, D., Engelbrecht, K., Bahl, C. R. H. & Bjork, R. Exploring the efficiency potential for an active magnetic regenerator. *Sci. Technol. Built Environ.* **22**, 527–533 (2016).
300. Lionte, S., Barcza, A., Risser, M., Muller, C. & Katter, M. LaFeSi-based magnetocaloric material analysis: cyclic endurance and thermal performance results. *Int. J. Refrig.* **124**, 43–51 (2021).
301. Rahman, S. et al. Pressure-induced structural evaluation and insulator-metal transition in the mixed spinel ferrite $Zn_{0.2}Mg_{0.8}Fe_2O_4$. *Phys. Rev. B* **95**, 024107 (2017).
302. Ueland, S. M. & Schuh, C. A. Surface roughness-controlled superelastic hysteresis in shape memory microwires. *Scr. Mater.* **82**, 1–4 (2014).
303. Steven Brown, J. & Domanski, P. A. Review of alternative cooling technologies. *Appl. Therm. Eng.* **64**, 252–262 (2014).
304. Cohen, L. F. Contributions to hysteresis in magnetocaloric materials. *Phys. Status Solidi B* **255**, 1700317 (2018).
305. Lovell, E., Pereira, A. M., Caplin, A. D., Lyubina, J. & Cohen, L. F. Dynamics of the first-order metamagnetic transition in magnetocaloric $La(Fe,Si)_{13}$: reducing hysteresis. *Adv. Energy Mater.* **5**, 1401639 (2015).
306. Moore, J. D. et al. Reducing the operational magnetic field in the prototype magnetocaloric system $Gd_5Ge_4$ by approaching the single cluster size limit. *Appl. Phys. Lett.* **88**, 072501 (2006).
307. Wu, S., Lin, M. R., Lu, S. G., Zhu, L. & Zhang, Q. M. Polar-fluoropolymer blends with tailored nanostructures for high energy density low loss capacitor applications. *Appl. Phys. Lett.* **99**, 132901 (2011).
308. Aziguli, H. et al. Tuning the electrocaloric reversibility in ferroelectric copolymers by a blend approach. *EPL* **125**, 57001 (2019).
309. Liu, Y., Haibibu, A., Xu, W. H., Han, Z. B. & Wang, Q. Observation of a negative thermal hysteresis in relaxor ferroelectric polymers. *Adv. Funct. Mater.* **30**, 2000648 (2020).
310. Fujita, A., Matsunami, D. & Yako, H. Realization of small intrinsic hysteresis with large magnetic entropy change in $La_{0.8}Pr_{0.2}(Fe_{0.88}Si_{0.10}Al_{0.02})_{13}$ by controlling itinerant-electron characteristics. *Appl. Phys. Lett.* **104**, 122410 (2014).
311. Zhang, H. et al. Reduction of hysteresis loss and large magnetocaloric effect in the C- and H-doped La(Fe, Si)$_{13}$ compounds around room temperature. *J. Appl. Phys.* **111**, 07A909 (2012).
312. Qiu, X., Hollander, L., Wirges, W., Gerhard, R. & Basso, H. C. Direct hysteresis measurements on ferroelectret films by means of a modified Sawyer–Tower circuit. *J. Appl. Phys.* **113**, 224106 (2013).

**Acknowledgements**
The authors acknowledge useful discussions with J. Cui, R. Radermacher, Y. Hwang, J. Muehlbauer, D. Catalini, D. Wen, R. Bao, Y. Xing, W. Yuan and L. Yuan. H.H. was supported by the National Natural Science Foundation of China (NSFC grant no. 12002013) and the Fundamental Research Funds for the Central Universities (grant no. 501LKQB2020105028). I.T. was supported by the U.S. Department of Energy under DE-EE0009159. S.Q. was supported by the National Natural Science Foundation of China (NSFC grant no. 51976149), the Young Elite Scientist Sponsorship Program by CAST (grant no. 2019QNRC001) and the China Postdoctoral Science Foundation (CPSF grant no. 2020M683471).

**Author contributions**
All authors contributed to the discussion of content, writing and editing of the manuscript prior to submission.

**Competing interests**
I.T. is a founder of Maryland Energy and Sensor Technologies, a company that works on elastocaloric technologies. The other authors declare no competing interests.

**Peer review information**
*Nature Reviews Materials* thanks Neil Mathur, Vitalij Pecharsky and the other, anonymous, reviewer(s) for their contribution to the peer review of this work.

**Publisher's note**
Springer Nature remains neutral with regard to jurisdictional claims in published maps and institutional affiliations.

**Supplementary information**
The online version contains supplementary material available at https://doi.org/10.1038/s41578-022-00428-x.

**RELATED LINKS**
**Refrigeration and airconditioning – Consumers:** http://www.environment.gov.au/protection/ozone/rac/consumers
**The Nobel Prize in Chemistry 1949:** https://www.nobelprize.org/prizes/chemistry/1949/summary/